UNSTEADY SLIP VELOCITY TO IMPROVE MASS TRANSFER IN SPIRAL WOUND REVERSE OSMOSIS MEMBRANE (SWM) SYSTEMS

LIANG YONG YEOW

RESEARCH VOTE NO:
RDU170324

Centre of Excellence for Advanced Research in Fluid Flow (CARIFF)
Universiti Malaysia Pahang

2019

DEDICATION

The authors acknowledge the funding support by Universiti Malaysia Pahang research grants (RDU170324). One of us (K.F) gratefully acknowledges scholarship funding by Universiti Malaysia Pahang (UMP).

Unsteady Slip Velocity To Improve Mass Transfer In Spiral Wound Reverse Osmosis Membrane (SWM) Systems

(***Keywords: CFD, Forced Slip Velocity, Mass Transfer, Concentration Polarisation***)

An unsteady forced slip velocity has an important effect on the flow conditions adjacent to the membrane interface, which can help control concentration polarisation (CP) and fouling. This study explores the effect of non-sinusoidal slip velocity waveforms on mass transfer and shear stress in membrane channels. The main finding of this is that a non-sinusoidal waveform with a sudden decrease in slip velocity for systems without vortex shedding, can significantly increase maximum shear stress (>20%). The second objective of this work is to compare oscillating flow and slip velocity mass transfer enhancement in spacer-filled membrane channels. One of this finding is that the mechanism by which the flow perturbations are generated is not as important as the perturbation frequency, in terms of increasing wall shear and permeate flux. The third objective of this work is to investigate the effect of SWM feed spacer geometry on mass transfer enhancement driven by forced transient slip velocity. One of the finding of this is that the resonant frequency is significantly affected by the interaction of the shear layer with successive downstream spacers, hence affecting the degree of mass transfer effectiveness.

Key Researchers:

Liang Yong Yeow

Foo Kathleen

Gustavo Fimbres Weihs

Dianne Wiley

David Fletcher

E-mail: yongyeow.liang@ump.edu.my

Tel. No: +6095492859

Vote No.: RDU170324

Halaju slip terpaksa yang tidak stabil untuk meningkatkan pemindahan jisim dalam modul membran *spiral-wound* (SWM)

(***Kata kunci: CFD, halaju slip terpaksa, pemindahan jisim, Polarisasi konsentrasi***)

Halaju slip terpaksa yang tidak stabil mempunyai kesan penting pada keadaan aliran yang bersebelahan antara muka membran, yang dapat membantu mengawal polarisasi konsentrasi (CP) dan kotoran. Kajian ini mengkaji kesan gelombang halaju slip kepada pemindahan jisim dan tegasan ricih dalam saluran membran. Hasil kajian mendapati gelombang bukan sinusoidal dengan penurunan secara mendadak dalam halaju slip untuk sistem tanpa tumpahan vorteks, dengan ketara boleh meningkatkan tekanan ricih maksimum (>20%). Objektif kedua kerja ini adalah untuk membandingkan aliran berosilasi dan halaju slip terpaksa dalam pemindahan jisim. Salah satu daripada penemuan ini adalah bahawa mekanisme di mana aliran dijana tidak sepenting frekuensi aliran, dari segi meningkatkan geseran dinding dan fluks. Objektif ketiga kerja ini adalah untuk mengkaji kesan geometri peruang SWM pada peningkatan pemindahan jisim yang didorong oleh halaju slip terpaksa yang tidak stabil. Salah satu penemuan ini adalah bahawa optima frekuensi erjejas dengan ketara oleh interaksi lapisan ricih di peruang hiliran.

Table of Contents

List of Figures

List of Tables

Nomenclature

Symbol

D	Solute diffusivity ($m^2\ s^{-1}$)
d_h	Hydraulic diameter (m)
E_x	Electric field component in the x-direction ($V\ m^{-1}$)
f_s	Frequency of oscillation of slip velocity (s^{-1})
F_s	Dimensionless frequency of oscillation of slip velocity
f	Friction factor
h_{ch}	Height of channel (m)
J	Permeate flux ($kg\ m^{-2}\ s^{-1}$)
L_{in}	Entrance length (m)
L_m	Membrane length (m)
L_{out}	Exit length (m)
L_p	Membrane permeance ($m\ s^{-1}\ Pa^{-1}$)
P	Pressure (Pa)
P_0	Dimensionless inlet transmembrane pressure
Δp_{tm}	Transmembrane pressure (Pa)
R	Membrane intrinsic rejection
$Re = \frac{\rho u_{eff} d_h}{\mu}$	Reynolds number
$Re_{s,RMS} = \frac{\rho u_{s,RMS} d_h}{\mu}$	RMS slip Reynolds number
t	Time (s)
$T=tf_s$	Dimensionless time
$T_s = \frac{1}{f_s}$	Slip velocity period
u	Local velocity in the x-direction ($m\ s^{-1}$)
$u_{eff} = u_{b0}/\varepsilon$	Effective velocity ($m\ s^{-1}$)
u_s	Slip velocity ($m\ s^{-1}$)
$u_{s,sq}$	Slip velocity ($m\ s^{-1}$) for square wave
$u_{s,tri}$	Slip velocity ($m\ s^{-1}$) for triangle wave
$u_{s,saw,1}$	Slip velocity ($m\ s^{-1}$) for sawtooth type with an instantaneous decrease in slip velocity
$u_{s,saw,2}$	Slip velocity ($m\ s^{-1}$) for sawtooth wave with an instantaneous increase in slip velocity
$u_{s,A}$	Oscillation amplitude of slip velocity ($m\ s^{-1}$)
$u_{s,RMS}$	Root mean square (RMS) of the time-dependent slip velocity over one sinusoidal cycle ($m\ s^{-1}$)
v	Local velocity in the y-direction ($m\ s^{-1}$)
w	Solute mass fraction
$X=x/h_{ch}$	Dimensionless distance in direction parallel to membrane surface
x	Distance in direction parallel to membrane surface (m)
y	Distance from membrane surface, in direction normal to the surface (m)

Greek letters

γ	Concentration polarisation index (modulus)
μ	Viscosity ($kg\ m^{-1}\ s^{-1}$)

π	Osmotic pressure (Pa)
$\pi_0 = \varphi w_{b0}$	Inlet osmotic pressure (Pa)
Π_{L_p}	Dimensionless membrane permeance
ρ	Fluid density (kg m^{-3})
σ	Reflection coefficient
φ	Osmotic pressure coefficient (Pa)
ε_e	Permittivity (F m^{-1})
ζ	Zeta potential (V)
τ	Wall shear stress (Pa)

Subscript

b0	Value at inlet bulk conditions
max	Value for maximum variable
TA	Value for time-averaged variable
w	Value on feed side membrane surface (wall)

CHAPTER 1. INTRODUCTION

1.1 State of the Art

To date, water scarcity is recognised as one of the greatest threats to human activity. With increased global water scarcity, membrane treatment technologies are becoming increasingly important as the most efficient technologies for purification and filtration [1]. The most common commercially available membrane modules are hollow fibre and spiral wound membranes (SWM), the latter of which is usually the choice for many industrial applications [2], especially for reverse osmosis (RO). One of the main problems that RO SWM modules face is concentration polarisation (CP). The adverse consequences of CP include the increase in osmotic pressure and the promotion of conditions that lead to membrane fouling, thus increasing the operating cost of a treatment plant and reducing the life span of membrane modules. CP can also lead to frequent cleaning or membrane module replacement [3].

1.2 Objective

The aim of the project is to minimize concentration polarization (CP) through unsteady slip flow perturbation. In order to achieve this aim, the following objectives are investigated:

1) To investigate the effect of unsteady slip velocity waveform on shear stress in membrane systems.
2) To compare oscillating flow and slip velocity mass transfer enhancement in spacer-filled membrane channels.
3) To investigate the effect of SWM feed spacer geometry on mass transfer enhancement driven by forced transient slip velocity.

1.3 Scope of the study

In order to achieve the objective of the study, the following scopes of the study are drawn:

1) Simulation of non-sinusoidal slip-velocity waveforms considered in this study are square, triangle and saw-tooth, as they are widely used in practice and can be easily coded into a signal generator.
2) CFD simulations of the membrane system performance under oscillating and forced-slip are compared at their resonant frequency. Then, the CFD simulations are carried out using a white noise input signal for both perturbation approaches (oscillating and

forced-slip) to test the possible occurrence perturbation amplification and vortex shedding.

3) To investigate the effect of SWM feed spacer geometry on mass transfer enhancement driven by forced transient slip velocity at *Re* 425.

CHAPTER 2.

CFD study of the effect of unsteady slip velocity waveform on shear stress in membrane systems

Y. Y. Liang[a,b*], *G. A. Fimbres Weihs*[c], *D. F. Fletcher*[d]

[a] Faculty of Chemical & Natural Resources Engineering, Universiti Malaysia Pahang, Lebuhraya Tun Razak, Gambang, Kuantan, 26300, Pahang, Malaysia
[b] Centre of Excellence for Advanced Research in Fluid Flow (CARIFF), Universiti Malaysia Pahang, Lebuhraya Tun Razak, Gambang, Kuantan, 26300, Pahang, Malaysia
[c] CONACyT–Instituto Tecnológico de Sonora, Antonio Caso & E. Kino, Cd. Obregón, Sonora, C.P. 85130, México
[d] The University of Sydney, School of Chemical and Biomolecular Engineering, NSW 2006, Australia

[*] Corresponding author. Tel.: +6095492859. E-mail: yongyeow.liang@ump.edu.my

Abstract

An unsteady forced slip velocity has an important effect on the flow conditions adjacent to a membrane interface, which can help control concentration polarisation (CP) and fouling. This study explores the effect of non-sinusoidal slip velocity waveforms on mass transfer and shear stress in membrane channels. The hydrodynamics and mass transfer of unobstructed and obstructed membrane channels under the influence of slip velocity are simulated using two-dimensional computational fluid dynamics (CFD). At a Reynolds number where vortex shedding occurs, the results show that both sinusoidal and non-sinusoidal slip velocity profiles cause a similar increase in mass transfer and shear stress. However, for systems without vortex shedding, a non-sinusoidal waveform with a sudden decrease in slip velocity can significantly increase maximum shear stress (by over 20 %). This effect shows a clear advantage of non-sinusoidal slip velocity profiles over sinusoidal slip velocity profiles.

Keywords: CFD, Slip velocity, Non-sinusoidal waveform, Mass transfer enhancement, Shear Stress

2.1 Introduction

The efficacy of reverse osmosis (RO) membrane operations is limited by concentration polarisation (CP) and fouling. Although reverse osmosis (RO) modules usually operate in steady-state, it has been demonstrated that unsteady operation can be beneficial in terms of energy requirements and operational cost [4].

The flow unsteadiness that is typically seen in RO processes can take the form of: 1) steady vortices 2) oscillations in the flow field and 3) laminar vortex shedding [5]. These types of flow unsteadiness can be obtained through the orientation and design of the spacer nets on the feed side of membrane module. This flow management approach might also be combined with other unsteady approaches to further minimise concentration polarisation and fouling, e.g. pulsatile pressure [6], mechanical mixing [7], low frequency ultrasound [8] and rotating/vibrating membranes [9]. All of these approaches control membrane fouling by manipulating the convective flow near the membrane surface and increasing the wall shear stress [10]. Out of these approaches, pulsatile pressure has been considered as a cost-effective method in terms of permeate flux enhancement for RO processes [4]. For example, Ali et al. [11] found that pulsatile pressure resulted in an increase in permeate flux of up to 42 % and a decrease in salt concentration in the permeate of about 20 %.

In designing an efficient membrane system, the distribution of local flow and shear stress near the membrane surface need to be taken into account. It has been shown elsewhere that a high shear stress is important for reducing the effect of fouling [12]. This is especially important during pulsatile flow [6, 13, 14], where a high-amplitude shear can help reduce fouling layer thickness. Maximum wall shear thus can be used as a proxy for long term fouling minimisation [15]. Shear stress can be characterised by two type of methods, namely experimental (e.g. particle image velocitmetry) and numerical (e.g. CFD) techniques [12]. CFD is increasingly being used as an analysis tool to provide insights into the flow behaviour in membrane systems, without the need to construct membranes or spacers [16]. Thus, CFD is used in this paper as a tool for analysing the hydrodynamics and mass transfer.

Simulation results show that perturbation of the flow inside the boundary layer can lead to a decrease in concentration polarisation and an increase in mass transfer [15, 17-19]. One way to disturb the flow near the membrane surface without accelerating the entire flow is through electro-osmotic flow (EOF), which is the motion of liquid near the membrane surface caused by an external electric field [17, 18]. The mathematical modelling of EOF can be simplified and mimicked by assuming a Helmholtz–Smoluchowski (HS) slip velocity [17]. It

is noteworthy to mention that since the HS slip velocity disrupts the boundary layer near the membrane surface, the simulation results obtained using this methodology are applicable to forced hydrodynamic perturbation of the boundary layer by any means (e.g. vibration [20]), not only for EOF.

In a previous study [19], we investigated the effect of the frequency of an oscillating slip velocity on the performance of a spacer-filled membrane system. It was found that for Reynolds numbers near the transition to unsteady flow (*Re* 408 – 536) [19], there exists a resonant frequency that induces vortex shedding, which ultimately maximises mass transfer enhancement and shear stress. Our previous work also showed that an oscillating slip velocity can reduce pumping power by about 36 %, while achieving the same flux as the case without a slip velocity.

Another important factor that affects the performance of forced transient inputs (i.e. forced unsteady flow) in RO modules is the shape of the waveform of the unsteady input (perturbation) [4]. It has been shown that pulsatile flow with a symmetric pressure square wave can generate a velocity profile with two equal maxima (bimodal) near the wall, rather than on the centreline, thus improving mixing and minimising concentration polarisation [4, 21]. Further, Al-Bastaki and Abbas [22] found that asymmetric square pressure pulses increase permeate flux by about 0.3 % to 13 % compared with steady-state operation, for the range of pulse amplitude (5 to 10 bars) and period (5 to 15 minutes) considered. This clearly indicates that the shape of the perturbation waveform can significantly affect the performance and efficiency of membrane systems.

For forced slip velocity, however, our previous study [19] only investigated sinusoidal waveforms, and the use of non-sinusoidal waveforms (e.g. square, triangle, sawtooth) has not yet been considered. Nonetheless, it is worth noting that any non-sinusoidal waveform can be represented by the summation of several frequency components, as expressed by a Fourier series expansion; hence, its response can be readily obtained from the sum of the responses to its individual components. Further, for membrane systems exhibiting linear dynamics, our previous work [15] shows that only the time-averaged value of the perturbation has an impact on the time-averaged flux, and the effect of the waveform of the perturbation is negligible. However, despite the fact that membrane channels without obstructions (spacers) behave as linear systems, a spacer-filled channel is not completely linear due to the wall-normal convection term caused by the interactions between the flow and the spacers [19]. For these

reasons, this paper aims to investigate the effect of non-sinusoidal input waveforms on mass-transfer enhancement for membrane channels.

This paper considers two cases: unobstructed (empty) and spacer-filled channels. The effect of a non-sinusoidal slip velocity is first analysed for empty channels, followed by the analysis of the more complex spacer-filled channel. This is because spacers introduce flow perturbations which could complicate the study of the transient effects alone [15]. Although the empty channel dynamic system is expected to be linear, the results from those simulations serve as a baseline for comparing the effect of non-sinusoidal slip in spacer-filled channels. Moreover, the empty channel case is also related to membrane operations without obstructions, e.g. hollow fibre RO [15].

The non-sinusoidal slip-velocity waveforms considered in this study are square, triangle and saw-tooth, as they are widely used in practice and can be easily coded into a signal generator. All waveforms are compared against a sinusoidal slip at the same root mean square slip velocity ($u_{s,\,RMS}$) [15]. Their effect on local and global mass transfer enhancement is emphasised with links to other pertinent parameters, such as the power number (a measure of energy loss) and maximum shear stress.

2.2 Problem description, assumptions and methods

2.2.1 Model description

The 2D transient Navier-Stokes and mass transfer equations are solved using commercial CFD software (ANSYS CFX-16.2), and their governing equations are described as follows:

$$\nabla \cdot \vec{v} = 0 \tag{1}$$

$$\rho \frac{\partial \vec{v}}{\partial t} + \rho(\vec{v} \cdot \nabla)\vec{v} = \mu \nabla^2 \vec{v} - \nabla p \tag{2}$$

$$\rho \frac{\partial w}{\partial t} + \rho \nabla \cdot (w\vec{v}) = D\nabla^2 w \tag{3}$$

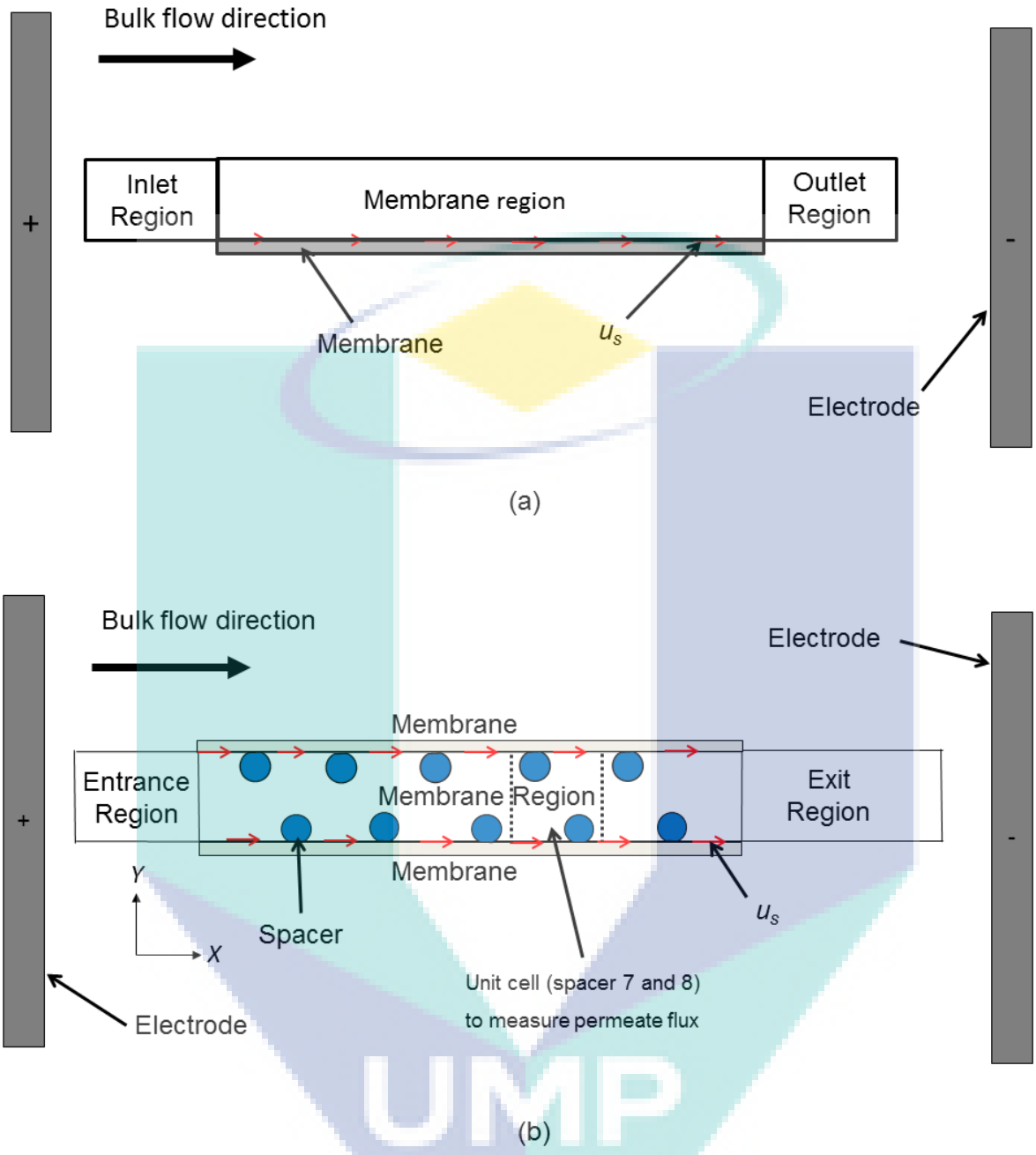

Figure 2.1: Schematic of fluid domain (not to scale) indicating boundary locations and channel regions for unobstructed (a) and obstructed channel (b). Red arrows on the membrane surface indicate the location of slip velocity [15, 19].

Figure 2.1a and b show the channel and electrode geometry for both unobstructed and obstructed channels, respectively. For obstructed channel, the unit cell containing the 7th and 8th spacer filaments (arrangement with $d_f/h_{ch} = 0.6$ and $l_m/h_{ch} = 4$ [19]) is selected for analysis of membrane performance [19]. The entrance and exit region are made long enough to prevent any interference between the entrance/exit region and the membrane region. For all simulations, the maximum Courant number was kept below 1, which resulted in convergence

for the time-averaged variables after approximately 100,000 to 800,000 time steps. A detailed description of the model geometry and assumptions can be found elsewhere [19].

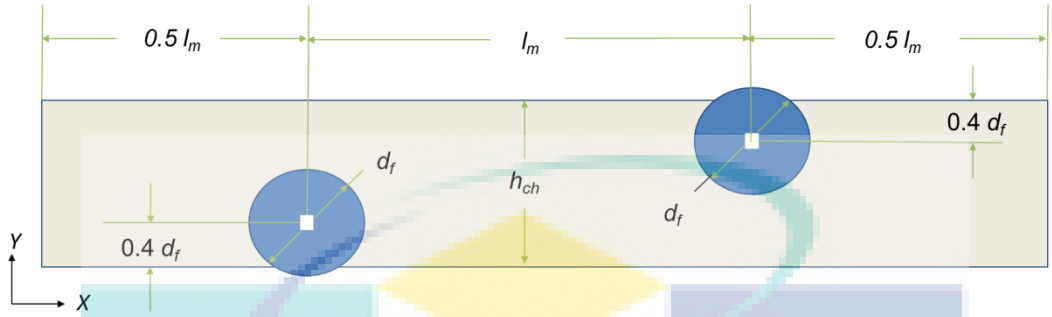

Figure 2.2: Geometry of the spacer unit cell of Figure 1b [19].

2.2.2 Boundary conditions

Both top and bottom membrane walls are considered as slip velocity conditions ($u = u_s$ and $v = v_w$). A Helmholtz-Smoluchowski slip velocity $\left(u_s = -\frac{\varepsilon_e \zeta E_x}{\mu}\right)$ of the order of 100 μm/s is used. This is representative of what the EOF velocity would be if using a typical electric field (E_x) employed in microchannels of the order of 10^4 V m^{-1}, considering the zeta potential (ζ) for RO membranes of the order of -10^{-2} V. The velocity normal to the membrane wall (v_w), which is equal to the permeate volumetric flux, is a function of local salt concentration following the Kedem-Katchalsky-Merten equation [23]:

$$v_w = \frac{J}{\rho} = L_p(\Delta p_{tm} - \sigma \varphi R w_w) \tag{4}$$

2.2.3 Assumptions and cases

The fluid under consideration is assumed to be incompressible and to have constant fluid properties (i.e. viscosity and diffusivity) [24, 25]. The fluid domain is discretised using a mesh with just over 2 million elements, which consists of at least 30 rectangular elements near the solid boundaries (approximately 2% of the channel height), and non-structured elements in the rest of the domain, each with maximum size of 1% of the channel height. Mesh-independence studies were carried out in order to ensure that the Grid Convergence Index (GCI) was below 5 % for both hydrodynamics and mass transfer; hence, the potential sources for errors in numerical calculations can be safely neglected.

The reference conditions for unobstructed and obstructed channels used in this work are presented in Table 2.1. The slip velocity waveforms for sinusoidal, square, triangle and sawtooth are depicted in Figure 2.3, and can be expressed by equations (5) to (9) respectively:

$$u_{s,sin} = u_{sin,A} \sin(2\pi f_s t) \tag{5}$$

$$u_{s,sq} = u_{sq,A}\left[2S\left(\sin(2\pi f_s t)\right) - 1\right]\mathrm{u_{s,t}} = -\frac{\varepsilon\xi\mathrm{E_x}}{\mu}\left[\mathrm{B} + \mathrm{A_{amp}}[\sin(2\pi\mathrm{ft})\right] \quad (6)$$

$$u_{s,tri} = u_{tri,A}\left\{2\left[2S\left(\sin(2\pi f_s t)\right) - 1\right]\left[1 - 2\frac{\mathrm{mod}(t,T_S)}{T_S}\right] - 1\right\} \quad (7)$$

$$u_{s,saw,1} = u_{saw,1,A}\left[2\frac{\mathrm{mod}(t,T_S)}{T_S} - 1\right]\mathrm{u_{s,t}} = -\frac{\varepsilon\xi\mathrm{E_x}}{\mu}\left[\mathrm{B} + \mathrm{A_{amp}}[\sin(2\pi\mathrm{ft})\right]\mathrm{u_{s,t}} = -\frac{\varepsilon\xi\mathrm{E_x}}{\mu}\left[\mathrm{B} + \mathrm{A_{amp}}[\sin(2\pi\mathrm{ft})\right] \quad (8)$$

$$u_{s,saw,2} = u_{saw,2,A}\left[1 - 2\frac{\mathrm{mod}(t,T_S)}{T_S}\right]\mathrm{u_{s,t}} = -\frac{\varepsilon\xi\mathrm{E_x}}{\mu}\left[\mathrm{B} + \mathrm{A_{amp}}[\sin(2\pi\mathrm{ft})\right]\mathrm{u_{s,t}} = -\frac{\varepsilon\xi\mathrm{E_x}}{\mu}\left[\mathrm{B} + \mathrm{A_{amp}}[\sin(2\pi\mathrm{ft})\right] \quad (9)$$

where t is time, T_S is the slip velocity period $\left(T_S = \frac{1}{f_S}\right)$, f_s is the oscillation frequency, mod(t, T_S) is the modulo (remainder) of the division of t by T_S, and $S(t)$ is the unit step function defined by:

$$S(t) = \begin{cases} 0 & , \quad t < 0 \\ 1 & , \quad t \geq 0 \end{cases} \quad (10)$$

Two types of sawtooth waveforms, namely $u_{s,saw,1}$ and $u_{s,saw,2}$ are investigated. The first one shows an instantaneous decrease in slip velocity followed by a gradual increase, whereas the latter shows an instantaneous increase in slip velocity followed by a gradual decrease. For the sake of simplicity, only a single value of f_s is used, corresponding to the peak frequency found in our previous work [19], i.e. $F_S = \frac{f_s h_{ch}}{u_{eff}} = 0.67$, for the Reynolds number 408 for the obstructed channel. The value of slip velocity amplitude (u_A) for the different waveforms is calculated so that they all have the same RMS slip velocity ($u_{s,RMS}$) [15]. Therefore, the amplitudes are related by:

$$u_{s,RMS} = u_{sq,A} = \frac{u_{tri,A}}{\sqrt{3}} = \frac{u_{saw,1,A}}{\sqrt{3}} = \frac{u_{saw,2,A}}{\sqrt{3}} = \frac{u_{sin,A}}{\sqrt{2}} \quad (11)$$

For simulations without spacers, computational times of the order of 100 h and more than 3 GB of memory on an 8-core Xeon Processor were required for each case. Simulations involving spacers, on the other hand, required larger computational times (of the order of 1000 h and more than 12 GB of memory for each case) on 48 cores of a high-performance computing cluster (University of Sydney's high-performance computing cluster Artemis).

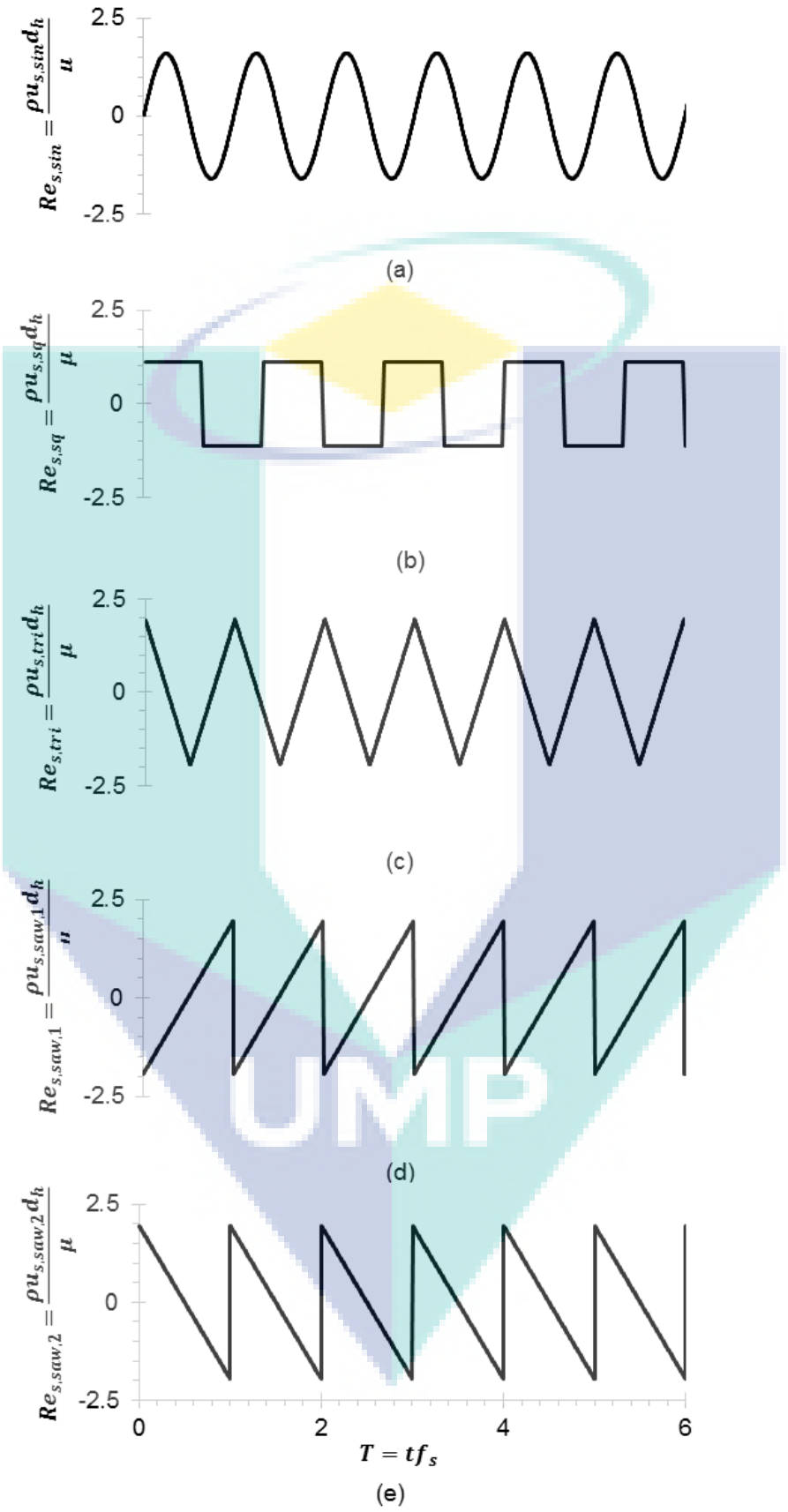

Figure 2.3: Time-series of slip velocity Reynolds numbers for the waveforms considered: (a) sinusoidal, (b) square, (c) triangle, (d) sawtooth 1, and (e) sawtooth 2.

Table 2.1: Parameters used for slip velocity case study.

Parameter	Value
Feed Solute Mass Fraction (w_{b0})	0.025
Dimensionless Inlet Transmembrane Pressure $\left(\boldsymbol{P_0 = \frac{\Delta p_{tm}}{\pi_0}}\right)$	1.46
Dimensionless Forced Slip Velocity Frequency $\left(\boldsymbol{F_s = \frac{f_s h_{ch}}{u_{eff}}}\right)$	0.67
Intrinsic Rejection (R)	0.996
Dimensionless Membrane Permeance $\left(\boldsymbol{\Pi_{L_p} = \frac{L_p \Delta p_{tm} d_h \rho}{\mu Re}}\right)$	1.27×10^{-3}
Reflection Coefficient (σ)	1
Reynolds number $\left(\boldsymbol{Re = \frac{\rho u_{eff} d_h}{\mu}}\right)$	408
RMS slip Reynolds number $\left(\boldsymbol{Re_{s,RMS} = \frac{\rho u_{s,RMS} d_h}{\mu}}\right)$	2

2.3 Methodology of analysis of results

Validation studies are crucial to establish reliability and accuracy of a model. The slip velocity CFD model used in this paper has been previously validated thoroughly with literature data both for steady-state and transient forced slip velocities [15, 26]. Moreover, the experimental requirements of the operations schemes considered in this work would necessitate a very high spatial resolution for visualising the slip velocity flow trend near the concentration polarisation boundary layer region. Therefore, direct experimental validation is not considered within the scope of the paper, as the main objective of this paper is to identify the most promising forced-slip waveforms for a later experimental study of the slip velocity effect in membrane systems.

The peak forced frequency of a typical membrane channel can be estimated using frequency response analysis [19], which requires the addition of a stimulus with a broad range of frequencies to the system (such as a pulse slip velocity). The frequency response is visualised by a plot of the amplitude ratio of an observed output (e.g. velocity) for a given stimulus, and can be calculated by dividing the magnitude of the Fourier transform of the observed output by the magnitude of the Fourier Transform of the pulse slip velocity input to the system. The frequency with the maximum amplitude ratio observed is referred to as the frequency response peak frequency (F_{pl}). Although frequency response analysis is only strictly applicable for linear systems, it was shown in our previous work that F_{pl} can approximate the actual peak frequency (F_{peak}) for a system with mild nonlinearity [19]. Thus, the F_{pl} value obtained from frequency response analysis is used in this paper as the frequency value at which the effect of the different slip velocity waveforms is analysed.

Transient simulations with a single-frequency sinusoidal slip-velocity input are carried out at F_{pl}, and the spatially local variables, time-averaged values (ϕ_{TA}) and maximum values ($\phi_{\max}$) are measured after the time-averaged variables have stabilised. The global variables ($\bar{\phi}$) are calculated as the area average of the local variables $\left(\bar{\phi} = \frac{1}{L}\int_L \phi\, dx\right)$ within the membrane region length of a unit cell (spacers 7 and 8) as shown in Figure 2.2.

Several dimensionless variables ($X = x/h_{ch}$ and $F_s = f_s h_{ch}/u_{eff}$) are used in this paper, following the methods used in our previous work [19]. Maximum wall shear stress $\left(\bar{\tau}_{\max} = \mu\left(\frac{\partial \bar{u}}{\partial y}\right)_{\max}\right)$, is measured as an indicator of long term fouling minimisation. This because larger instantaneous shear rates tend to reduce the effect of fouling [15]. The Power number ($Pn = Re^3 f_{TA}$) is used as a proxy measure of energy losses [19] for the different slip velocity waveforms.

2.4 Results and Discussion

2.4.1 Empty channel

As discussed in our previous work [15], the system described by the hydrodynamics and mass transfer is linear for an empty (unobstructed) channel. This implies that the effect of oscillations in variables such as pumping energy, concentration polarisation and permeate flux are nullified within the oscillation period. Nevertheless, we showed that unsteady slip velocity has a significant impact on the maximum wall shear stress. This section therefore investigates the effect of the different slip velocity waveforms on the maximum wall shear in an empty channel.

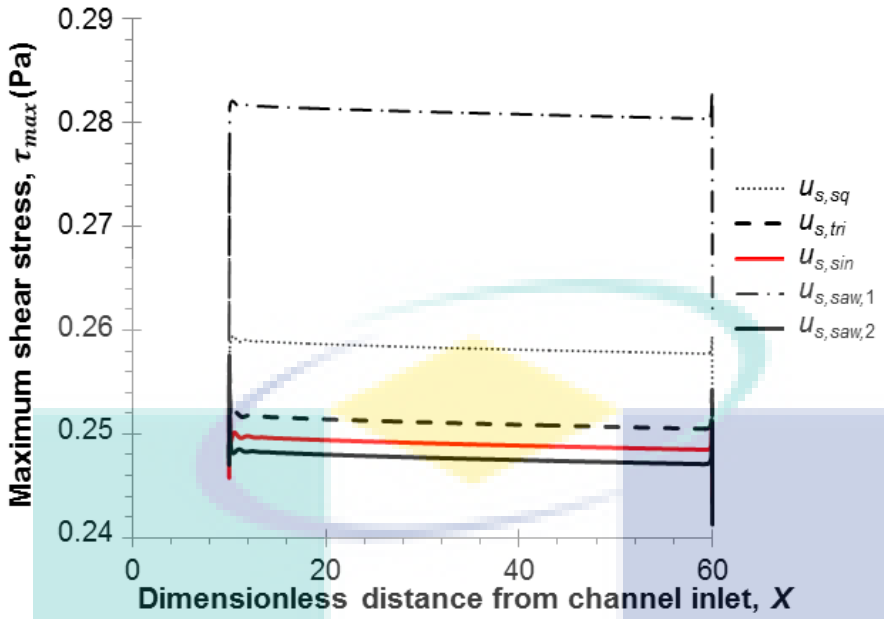

Figure 2.4: Maximum local shear stress profile along the membrane surface for different waveform of unsteady slip velocity at $F_s = 0.67$.

Figure 2.4 shows the effect of unsteady slip velocity along the membrane surface on the maximum wall shear. It shows that $u_{s,saw,1}$ causes the largest maximum wall shear, followed by $u_{s,sq}$, $u_{s,tri}$, $u_{s,sin}$ and finally $u_{s,saw,2}$. This is because, as shown in Figure 2.5, a sudden decrease in slip velocity causes maximum shear. Further, Figure 2.3 shows that the sudden decrease in slip velocity for the sawtooth 1 waveform ($\Delta Re_s \approx -3.9$) has a larger magnitude than the sudden decrease for the square waveform ($\Delta Re_s \approx -2.3$), which explains why the sawtooth 1 waveform presents the largest maximum wall shear. Figure 2.5 also shows that the maximum shear for all types of slip velocity occurs at the minimum slip velocity and vice versa, which agrees with our previous finding that shear rate decreases linearly as the slip velocity increases in the direction of bulk flow [15].

Table 2 summarises the comparison between the results from different slip velocity waveforms and no-slip in terms of maximum shear stress. As shown in this table, $u_{s,saw,1}$ shows the largest increase in maximum wall shear (17.33 % higher than the case with no-slip). Given that a higher maximum shear rate minimises the effect of fouling, this represents an advantage for non-sinusoidal waveforms with a sudden decrease in slip velocity, i.e. $u_{s,saw,1}$ and $u_{s,sq}$. Although this effect is consistent with a linear system, for a nonlinear system (e.g. an obstructed channel) [19] the effect of a non-sinusoidal slip velocity on maximum shear and mass transfer enhancement may be different. Those effects are the focus in the next section.

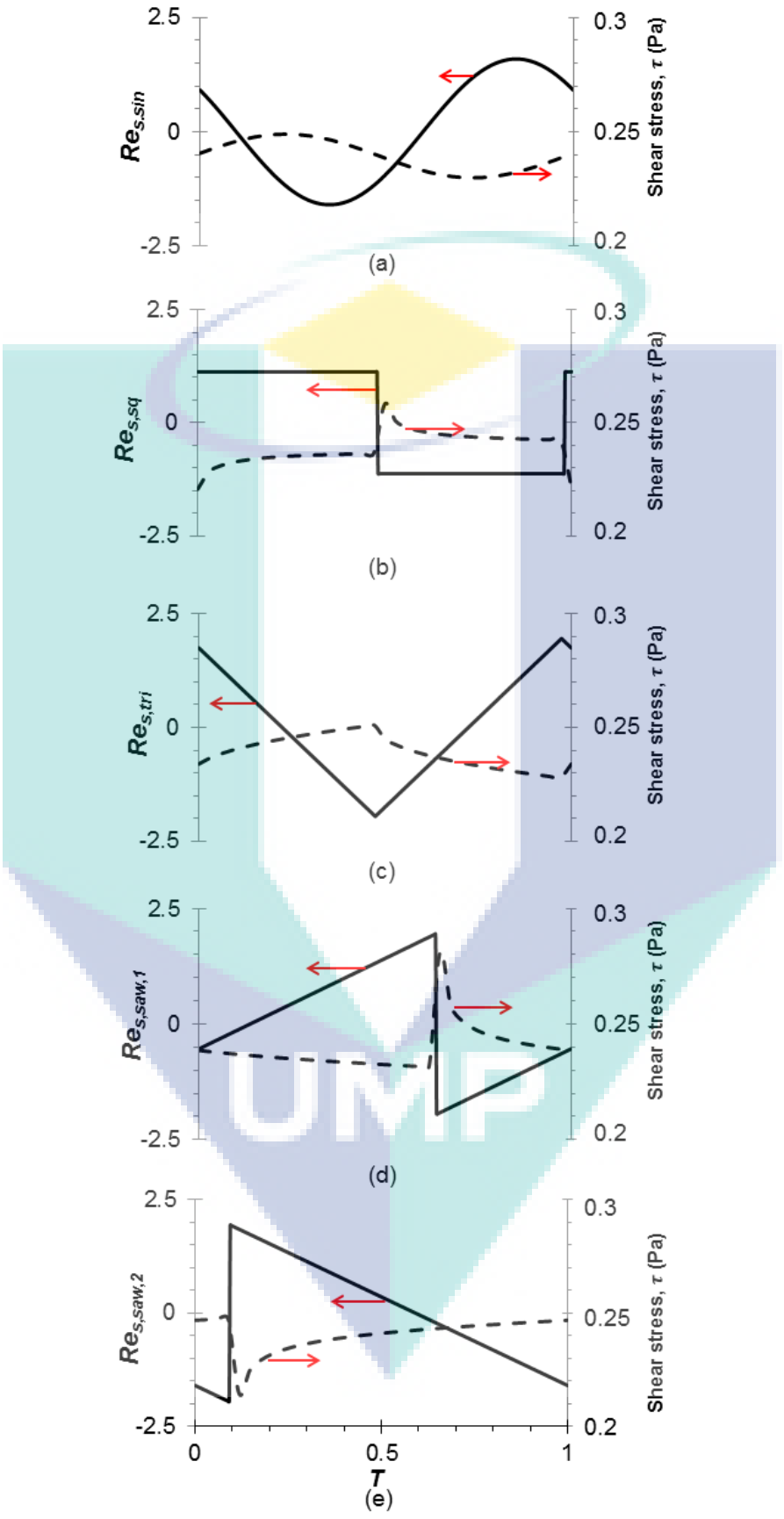

Figure 2.5: Effect of slip velocity time-series on wall shear stress for (a) $u_{s,sin}$ (b) $u_{s,sq}$ (c) $u_{s,tri}$ (d) $u_{s,saw,1}$ (e) $u_{s,saw,2}$ at $X = 35$.

Table 2.2: Comparison of the effect of slip velocity waveform against case with no-slip, in terms of wall shear stress ($\bar{\tau}_{\max}$) in empty channel.

Slip velocity waveform	$\Delta\bar{\tau}_{\max}$ (%)
$u_{s,sin}$	4.00
$u_{s,sq}$	7.86
$u_{s,tri}$	4.83
$u_{s,saw,1}$	17.33
$u_{s,saw,2}$	3.41

2.4.2 Spacer-filled channel

For spacer-filled membrane channels, it is important to note that both sets of spacer filaments (on both the top and bottom membrane) experience each sawtooth waveform in the same manner. The difference between the two sawtooth waveforms is that sawtooth 1 accelerates gradually and decelerates suddenly, whereas sawtooth 2 accelerates suddenly and decelerates gradually. The acceleration and deceleration are in the direction of the bulk flow (in the positive *x*-direction), whereas the shear rate ($\partial u/\partial y$) are in the direction normal to the membrane (positive *y*-direction for the top spacer and negative *y*-direction for the bottom membrane). As the top and bottom spacers are only flipped in the *y*-direction, this means that the direction of the acceleration and deceleration experienced by both the top and bottom spacers is the same, but the sign of the shear rate is changed. Hence, both sets of spacers (top and bottom) will experience the acceleration/deceleration cycle of each sawtooth waveform in the same way, and different between sawtooth 1 and 2. However, the mass transfer effect for all waveforms was found to be similar, without any significant differences between waveforms.

Table 2.3: Comparison of the effect of slip velocity waveform against case with no-slip in a spacer-filled channel for Re = 408.

Slip velocity waveform	$\Delta\bar{J}_{TA}$ (%)	ΔPn_{TA} (%)	$\Delta\bar{\tau}_{\max}$ (%)
$u_{s,sin}$	18.27	7.83	148.51
$u_{s,sq}$	18.03	5.12	146.14
$u_{s,tri}$	18.32	6.57	148.32
$u_{s,saw,1}$	17.68	6.01	142.47

As shown in Table 2.3, all the non-sinusoidal forced-slip waveforms lead to similar increases as a sinusoidal forced-slip in maximum shear (around 145 %), time-averaged flux (around 18 %) and pumping energy (around 6 %). This is because, as shown in Figure 2.6b,

the amplitude of oscillation of wall shear is similar for all waveforms under consideration within the unit cell (7th and 8th filaments). In addition, the effect of sinusoidal and non-sinusoidal forced-slip waveforms on the velocity field and solute concentration are also similar, as shown in Figure 2.7.

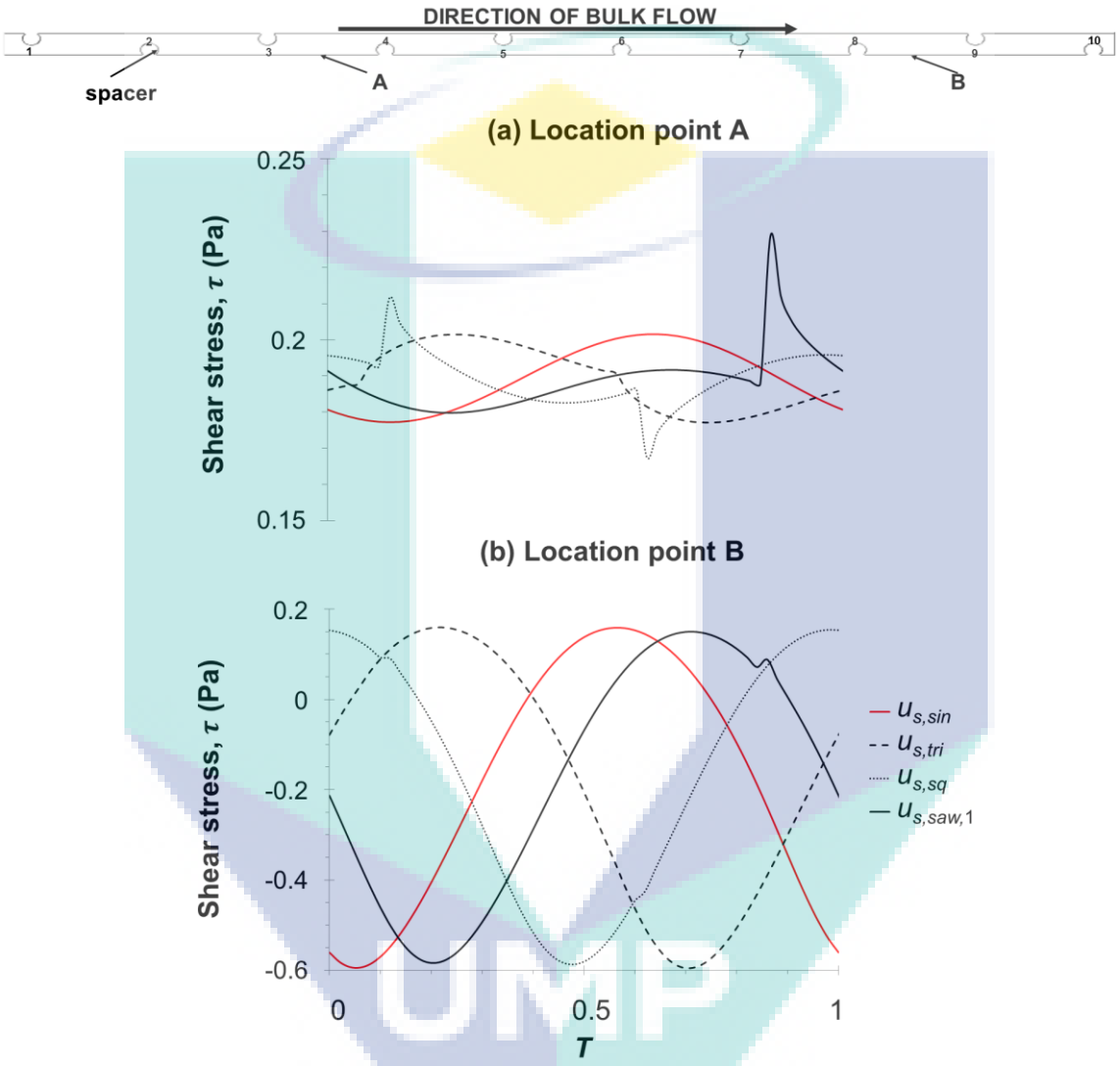

Figure 2.6: Time series wall shear profile at location A (region without vortex shedding (a)) and B (region with vortex shedding (b)) for $u_{s,sin}$, $u_{s,sq}$, $u_{s,\mathrm{tri}}$ and $u_{s,saw,1}$ at Re = 408.

Conversely, at the upstream region where vortex shedding is not yet developed, it can be observed that the wall shear tends to follow the shape of the respective slip velocity waveform (Figure 2.6a). These results suggest that non-sinusoidal waveforms are only more efficient in terms of maximum wall shear for flow without vortex shedding. The results shown in Table 2.4 confirm this effect for a lower Reynolds number of Re 200 (no vortex shedding), showing the relative increase in wall shear from the no-slip case when a slip velocity is applied

at the corresponding peak frequency for that Reynolds number (F_{pl} = 0.58) obtained from the frequency response.

Table 2.4: Comparison of the effect of slip velocity waveform against the case with no-slip, in terms of maximum wall shear increase ($\Delta\bar{\tau}_{max}$) in a spacer-filled channel for Re = 200 with F_{pl} = 0.58.

Slip velocity waveform	$\Delta\bar{\tau}_{max}$ (%)
$u_{s,sin}$	6.70
$u_{s,sq}$	11.43
$u_{s,tri}$	7.99
$u_{s,saw,1}$	20.88

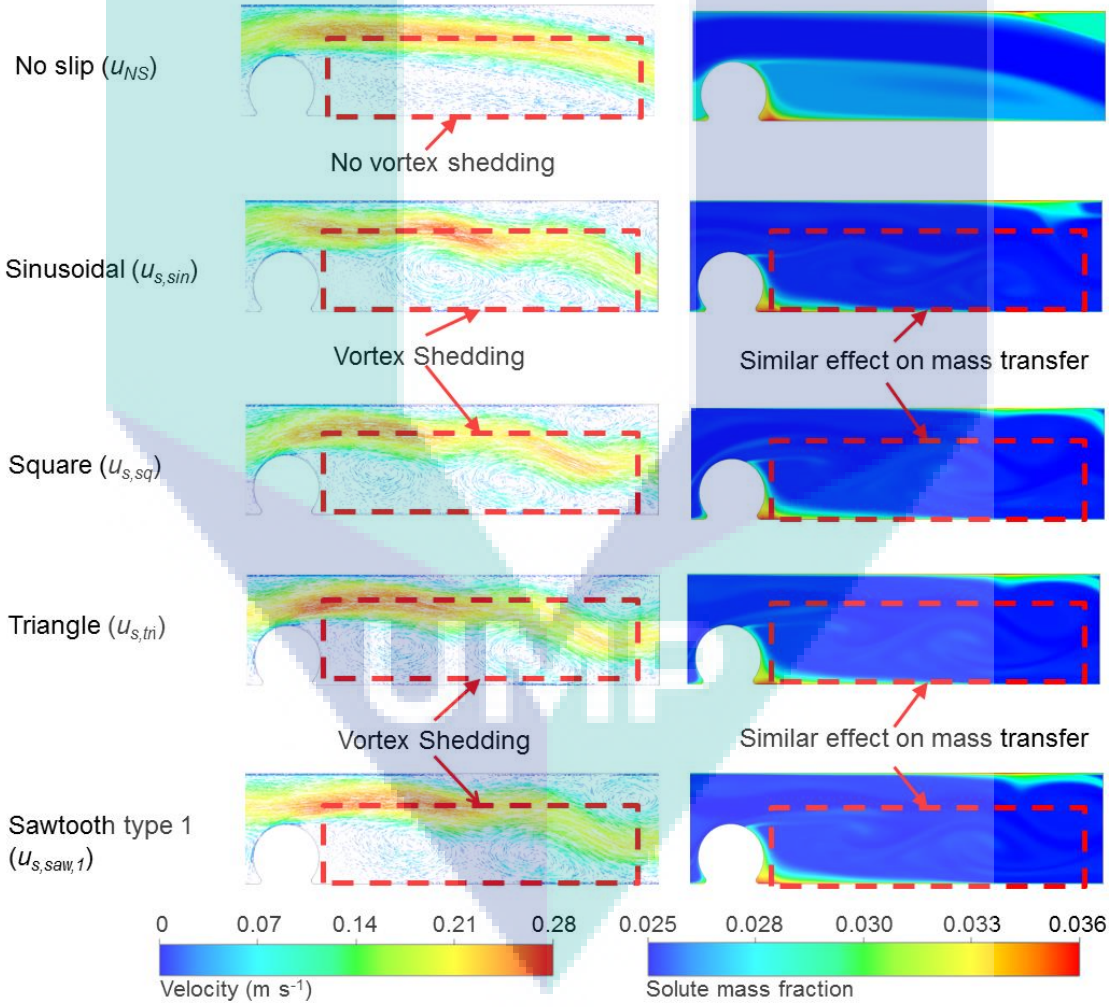

Figure 2.7: Effect of slip velocity waveform on the velocity field and solute concentration in the region within spacer 8 for Re 408

The results in Figure 2.7 demonstrate that non-sinusoidal forced-slip can be used to induce vortex shedding flow, even though other frequency components are present in the non-

sinusoidal forced-slip. This is because most of the effect of the perturbation is associated with the frequency component that corresponds to the peak frequency (F_{peak}) found previously for the sinusoidal waveform [19]. This is further supported by the results shown in Figure 2.6b, where it can be seen that the wall shear for non-sinusoidal waveforms tends to have a sinusoidal shape, regardless of slip velocity waveform, although small perturbations to the sinusoidal wall shear are observed for $u_{s,sq}$ and $u_{s,saw,1}$ due to sudden increases or decreases in slip velocity.

2.5 Conclusions

This paper compares the effect of non-sinusoidal slip velocity against sinusoidal slip velocity at the same RMS slip velocity in unobstructed and obstructed channels. At the Reynolds number where vortex shedding occurs, non-sinusoidal slip velocity waveforms did not show significant differences to a sinusoidal slip velocity, in terms of both mass transfer rate and wall shear. This is because vortex shedding controls the mass transfer rate and wall shear, and its occurrence only depends on the peak frequency component of any non-uniform slip velocity, rather than on their waveform.

However, for lower Reynolds numbers where there is no vortex shedding, non-sinusoidal waveforms with a sudden decrease in slip velocity lead to an increase in maximum wall shear. Therefore, these types of waveforms might be particularly suited for maximising wall shear for systems with low Reynolds number (e.g. high viscosity or low feed flow rate systems). It may be possible that other techniques (i.e. vibration) can also be used for generating forced velocity in the vicinity of membrane surface to improve mixing and mass transfer enhancement.

The results presented in this paper show that the maximum shear is larger for waveforms with sudden decrease in slip velocity. The cases considered in this study are only two-dimensional, so future work should consider extending the current simulations to three-dimensional cases, as greater slip velocity mass transfer enhancement might be observed due to the occurrence of transverse flow instabilities.

Acknowledgements

The authors acknowledge the Sydney Informatics Hub and the University of Sydney's high performance computing cluster Artemis for providing the high performance computing resources that have contributed to the research results reported within this paper. Funding support by Universiti Malaysia Pahang research grants (Project numbers RDU160342, RDU170324 and PGRS170341), the Cátedras CONACYT Program (Project 2338) and Instituto Tecnológico de Sonora (PROFAPI fund Project 2018-0029) is also acknowledged.

UMP

CHAPTER 3

Comparison of oscillating flow and slip velocity mass transfer enhancement in spacer-filled membrane channels: CFD analysis and validation

Y. Y. Liang[a,b], *G. A. Fimbres Weihs*[c,d*], *D. E. Wiley*[d]

[a]Faculty of Chemical and Natural Resources Engineering, Universiti Malaysia Pahang, Lebuhraya Tun Razak, 26300 Gambang, Kuantan, Pahang
[b]Centre of Excellence for Advanced Research in Fluid Flow (CARIFF), Universiti Malaysia Pahang, Lebuhraya Tun Razak, 26300 Gambang, Kuantan, Pahang, Malaysia
[c]CONACyT–Instituto Tecnológico de Sonora, 5 de Febrero 818 Sur, Cd. Obregón, Sonora, C.P. 85000, México
[d]School of Chemical and Biomolecular Engineering, The University of Sydney, NSW 2006, Australia

[*] Corresponding author. T: +61 2 9351 2854, E: gustavo.fimbresweihs@sydney.edu.au

Abstract

Unsteady shear methods have the potential to generate flow perturbations near the membrane surface, which play an important role in reducing concentration polarisation and fouling tendency. In general, there are two main approaches for generating time-varying flow perturbations: 1) generating oscillations in the bulk flow; or 2) forcing a slip velocity near the membrane surface. This paper presents a detailed comparison study of both approaches by means of two-dimensional computational fluid dynamics (CFD) simulations. The results show that both approaches result in significant increases in flux and maximum wall shear at the same disturbance resonant frequency and Reynolds number. This suggests that the mechanism by which the flow perturbations are generated is not as important as the perturbation frequency, in terms of increasing wall shear and permeate flux. However, it is more important to perturb flow near the membrane surface because it reduces energy consumption compared to oscillating flow approach. In addition, this paper confirms that a white noise perturbation can be used to simplify the approach for maximising vortex-shedding-induced mass transfer enhancement, without the need to identify the peak/resonant frequency for the flow in spacer-filled membrane channels at the expense of a higher pressure loss.

Keywords: CFD; flow perturbation; slip velocity; oscillating flow; white noise perturbation

3.1 Introduction

Unsteady shear techniques have been recognised as an effective way to reduce the thickness of the boundary layer adjacent to a membrane, thereby enhancing permeate flux [27]. There are two main mechanisms by which unsteady flow enhances flux: a) by increasing wall shear, thus decreasing the concentration boundary layer thickness; and b) by causing flow of low concentration fluid to the concentration boundary layer, thus promoting boundary layer renewal [28]. In general, there are two methods for increasing shear on the membrane surface: 1) periodically increasing the bulk cross flow velocity, e.g. oscillating flow [6]; and 2) promoting a change in the velocity of the fluid relative to the bulk flow (i.e. a "forced-slip") in the vicinity of the boundary layer, e.g. rotating/vibrating membranes [9], electro-osmotic flow (EOF) mixing [19]. Of these approaches, oscillating flow has been recognized as a cost-effective approach for membrane operations [4]. However, the main drawback of oscillating flow is that it may not be energy-efficient in causing a significant effect on the concentration gradient in the boundary layer, because it accelerates the bulk flow more than the flow near the membrane surface [4]. Moreover, high pressure oscillating flow tends to promote the development of scaling [29].

The forced slip velocity approach, on the other hand, focuses on promoting the motion of the fluid with respect to an adjacent surface, resulting from either applied mechanical vibration [9] or by making use of electro-osmosis via the application of an external electric field [3, 18]. A comparative benefit of this latter approach is that a smaller volume of fluid needs to be forced to move to generate a similar increase in shear, thus potentially requiring less energy. Computational Fluid Dynamics (CFD) studies [15, 17-19] of forced-slip flux enhancement have found that this approach has the potential to significantly increase the productivity of membrane systems by disrupting the concentration boundary layer, due to the movement of a thin layer of fluid adjacent to the membrane surface. The main similarities and differences between the oscillating and forced-slip approaches in terms of direction of perturbation, driving force and flux mechanisms are summarised in Table 3.1.

Table 3.1: Comparison of main features between oscillating and forced-slip approach

Feature	Oscillating flow approach [30]	Forced-slip approach [19]
	Differences	
Direction of perturbation flow	Flow perturbations caused at the membrane entrance are carried downstream the membrane channel	Flow perturbations occur everywhere along the membrane surface
Driving force	Pressure only	Pressure and mechanical vibration/electric field
	Similarities	
Flux enhancement mechanism	There is a resonant perturbation frequency that induces vortex shedding, which ultimately leads to boundary layer renewal and improved flow mixing	

Although both the oscillating and forced-slip approaches show promising potential for inducing vortex shedding [19, 30], there is no clear understanding on the extent to which each approach can further improve flux and wall shear. Moreover, the promotion of vortex shedding mainly depends on the accurate identification of the resonant perturbation frequency for a particular flow in spacer-filled channels. One way to estimate the resonant or "peak" frequency (i.e. the frequency that leads to a peak in the response) of the flow in a spacer-filled channel is the use of frequency response analysis. This analysis can be carried out by adding a stimulus to the flow system in order to obtain the amplitude ratio, i.e. the ratio of the amplitude of the observed output (e.g. the velocity at some point in the spacer-filled channel) with respect to the amplitude of the input stimulus. Using Fourier analysis, the amplitude ratio for a range of frequencies can be determined with a single test [31]. Thus, the frequency that results in the maximum amplitude ratio is termed the peak frequency.

Further, it may be possible to induce vortex shedding at Reynolds numbers for which normally steady-state flow is observed, using a white noise perturbation. A white noise perturbation that presents equal intensity over a range of frequencies (presumably including the resonant frequency) may be generated experimentally using a digital signal processor or microcontroller. The main advantage of this approach is that, because the white noise input contains a range of frequency components, the spacer-filled channel would preferentially react to its resonant frequency and there is no need to identify the peak frequency a-priori. However, it is unclear whether the other frequency components present in the white noise signal would hinder mixing in the channel. This paper therefore aims to test the white noise flux-enhancement approach, under both flow and forced-slip perturbations.

The study is organised as follows. First, CFD simulations of the membrane system performance under oscillating and forced-slip are compared at their resonant frequency. The analysis of these data can help determine any effects related to the source of perturbation (in the bulk flow vs. near the membrane wall) on mass transfer enhancement. The CFD results obtained from the forced-slip and oscillating flow are compared against the experimental data for oscillating flow in order to establish proof-of-concept of the improved flux due to unsteady disturbance in real life. Secondly, the CFD simulations are carried out using a white noise input signal for both perturbation approaches (oscillating and forced-slip) to test the possible occurrence perturbation amplification and vortex shedding.

3.2 Problem description, assumptions and methods

3.2.1 Model description

The commercial code ANSYS CFX-16.2 is used for the simulation studies presented in this paper. The governing equations (continuity, momentum and mass transfer) to be solved are:

$$\nabla \bullet \vec{\mathbf{v}} \tag{1}$$

$$\rho \frac{\partial \vec{\mathbf{v}}}{\partial t} + \rho \left(\vec{\mathbf{v}} \bullet \nabla \right) \vec{\mathbf{v}} = \mu \nabla^2 \vec{\mathbf{v}} - \nabla \rho \tag{2}$$

$$\rho \frac{\partial w}{\partial t} + \rho \nabla \bullet \left(w \vec{\mathbf{v}} \right) = D \nabla^2 w \tag{3}$$

For forced slip velocity simulations, the channel under consideration is illustrated in Figure 3.0.1. Oscillating flow simulations, on the other hand, use the same channel and spacer geometry as the forced slip velocity case, but with an inlet velocity that oscillates in time. Both slip velocity and oscillating flow approaches use a spacer arrangement with $d_f/h_{ch} = 0.6$ and $l_m/h_{ch} = 4$ (Figure 3.0.2), as this geometry has been shown to perform better than other combinations [19, 32]. A unit cell containing the 7th and 8th spacer is chosen as representative of the full length channel for measurement of hydrodynamic and mass transfer variables. A range of Reynolds numbers (*Re*) from 300 to 400 is used in this study, as they are typical recommended operating conditions for commercial SWM modules [33-35]. Furthermore, it has previously been found that at these Reynolds number, unsteady forced flow has the potential to induce vortex shedding [19, 36].

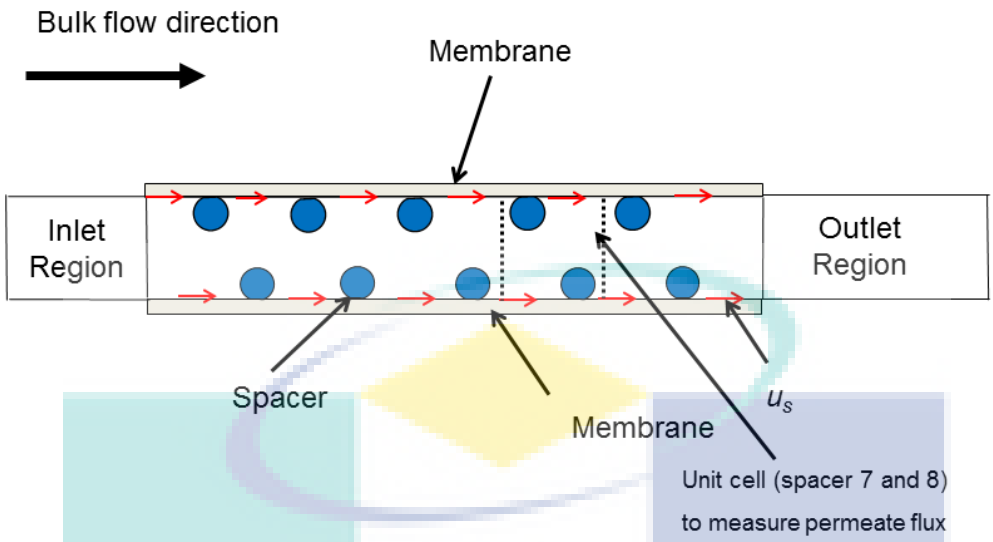

Figure 3.0.1: Schematic of fluid domain indicating boundary locations, not to scale (as in [19]).

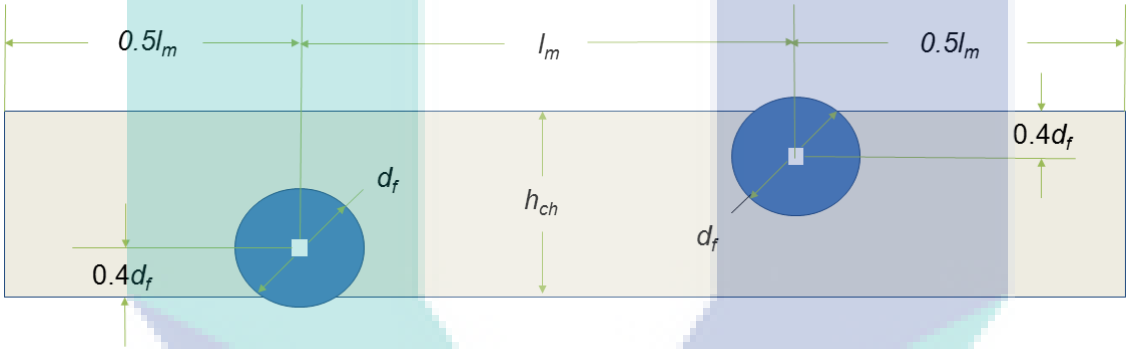

Figure 3.0.2: Geometry of the spacer unit cell (as in [19]).

3.2.2 Boundary conditions

Both top and bottom membrane wall boundary conditions were modelled as permeation with slip velocity. The velocity normal to the wall (v_w) is computed based on the Kedem-Katchalsky equation [23]:

$$v_w = -\frac{J}{\rho} = -L_p\left(\Delta p_{tm} - \sigma\varphi R w_w\right) \tag{4}$$

The forced slip velocity approximation is implemented as a moving wall ($u_w = u_s$), as in our previous work [17]. In order to induce transient perturbations in the forced slip velocity simulations, a sinusoidal forced-slip is incorporated using equation (5) at the membrane walls. For the oscillating flow simulations, flow disturbances at the inlet are incorporated as expressed by equation (6).

$$U_s(t) = \frac{u_{s,A}}{u_{eff}} \sin\left(2\pi f_p t\right) \tag{5}$$

$$U_{b0}(t) = \frac{u_{b0}}{u_{eff}} \left[1 + U_{b0,A} \sin\left(2\pi f_p t\right)\right] \tag{6}$$

where t, f_p, $u_{s,A}$, u_{b0}, $U_{b0,A}$ refer to time, perturbation frequency, slip velocity amplitude, feed velocity and fractional change in oscillating feed flow respectively. The values of f_p used in this paper are the same as the oscillating flow resonant frequencies found by previous studies [36, 37] to induce vortex shedding and maximise permeate flux for each particular value of Re.

3.2.3 Assumption and cases

The fluid is treated as incompressible and its properties are assumed to be constant. Following our previous work [38], convergence criteria of RMS errors below 10^{-5} and an RMS Courant number below 1 were specified for each time step, in order to ensure the accuracy of the hydrodynamic and mass transfer results. In addition, an unstructured grid with over 2 million elements used in our previous work [38, 39] is employed, giving a grid convergence index (GCI) below 5% for all variables of interest.

The dimensionless parameters used for both slip velocity and oscillating flow simulations are shown in Table 3.2. The slip Reynolds number (Re_s) is obtained by using the value of slip velocity ($u_{s,A}$). All the simulation runs reported in this paper require large computational times (of the order of 1,000 h and more than 12 GB of memory for each case) on 48 cores of a high-performance computing cluster (University of Sydney's high-performance computing cluster Artemis).

Table 3.2: Parameters used for both slip velocity and oscillating flow simulations.

Parameter	**Value**
Dimensionless Inlet Transmembrane Pressure ($P_0 = \Delta p_{tm} / \pi_0$)	1.46
Dimensionless perturbation frequency ($F_p = f_p\, h_{ch} / u_{eff}$)	0.6
Dimensionless membrane permeance ($\Pi_{Lp} = L_p\, \Delta p_{tm}\, d_h\, \rho / \mu$)	1.42×10^{-3}, 1.62×10^{-3}
Feed Solute Mass Fraction (w_{b0})	0.025
Fractional change in oscillating feed flow ($U_{b0,A}$)	0.05
Intrinsic Rejection (R)	0.996
Reflection Coefficient (σ)	1
Reynolds number ($Re = \rho\, u_{eff}\, d_h / \mu$)	350, 400, 600
Slip Reynolds number ($Re_s = \rho\, u_{s,A}\, d_h / \mu$)	2

3.2.4 Experimental cases

In order to serve as a proof-of-concept for oscillating flow mass transfer enhancement, pressure disturbances were introduced to a cross-flow system by means of an oscillating valve at different frequencies (from 5 Hz to 30 Hz). Brackish water with a concentration of 10,000 ppm sodium chloride (NaCl) and a commercial reverse osmosis membrane (Dow Filmtec BW30) were used in a cross-flow module (Sterlitech CF042). A commercial non-woven ladder-type spacer mesh (34 mil, h_{ch} = 0.86 mm, l_m/h_{ch} = 3.3) obtained from a Dow Filmtec spiral wound module (see Figure 3.0.3), was placed inside the cross-flow cells to induce interactions with the oscillating flow. The filaments of the spacer were oriented at 45° relative to the bulk flow direction, as this configuration is comparable to the zigzag geometry used in the 2D CFD simulation. Nonetheless, the analogy between the 45° 3D and 2D zigzag spacers is not an exact match [5], and differences in the hydrodynamic and mass transfer characteristics of the spacer-filled channel are to be expected. Therefore, the comparison between numerical and experimental results is not used to validate the numerical model, but only to provide proof of the concept of flux increase at certain frequencies of oscillation.

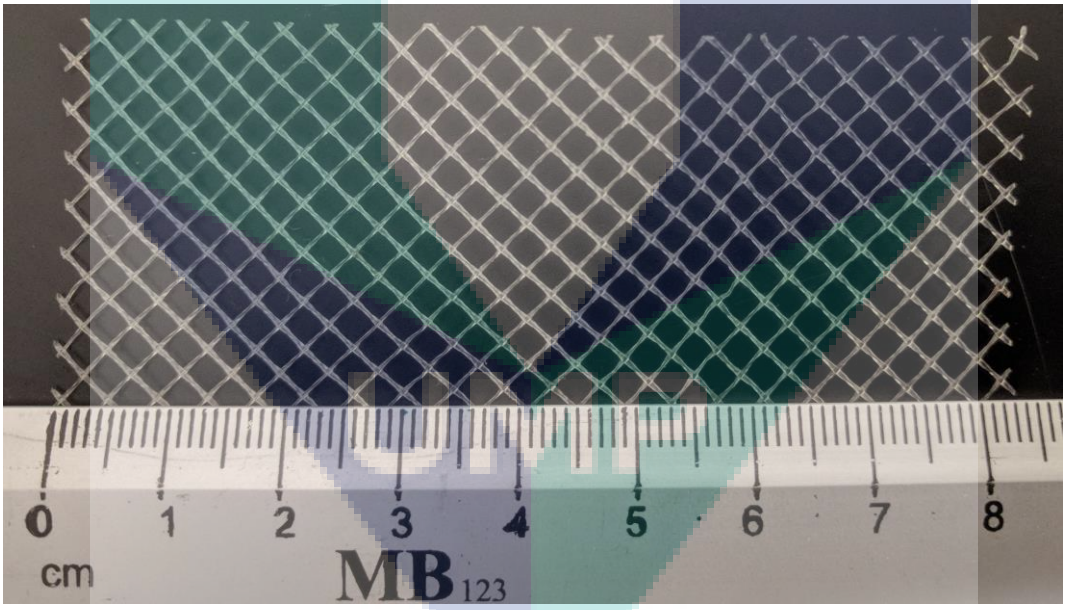

Figure 3.0.3: Photograph of the commercial spacer mesh (34 mil) used in the experimental tests.

Tests were carried out at different valve oscillation frequencies to observe the effect of frequency on permeate flux. The temperature of the feed water was controlled by a heat exchanger and a cooling system (PolyScience Benchtop Chiller LS5) and kept between 26 °C and 30 °C. The pressure varied between 4 and 6 MPa. Figure 3.0.4 shows the piping and instrumentation diagram of the laboratory scale cross-flow system used in this paper. Pressure, volumetric flow, conductivity and temperature data were collected for all flows using electronic

sensors. The permeate was measured using a precision electronic scale (OHaus Adventurer Pro AV4101C). For the generation of disturbances, an oscillating valve (see Figure 3.0.5) was designed, built and connected to the retentate line of the cross-flow modules, to induce oscillatory flow in the system. The valve mechanism works by periodically widening and narrowing an internal channel, the frequency/periodicity of which is controlled by the rotational speed of the motor attached to the valve. This design allows testing at different oscillation frequencies.

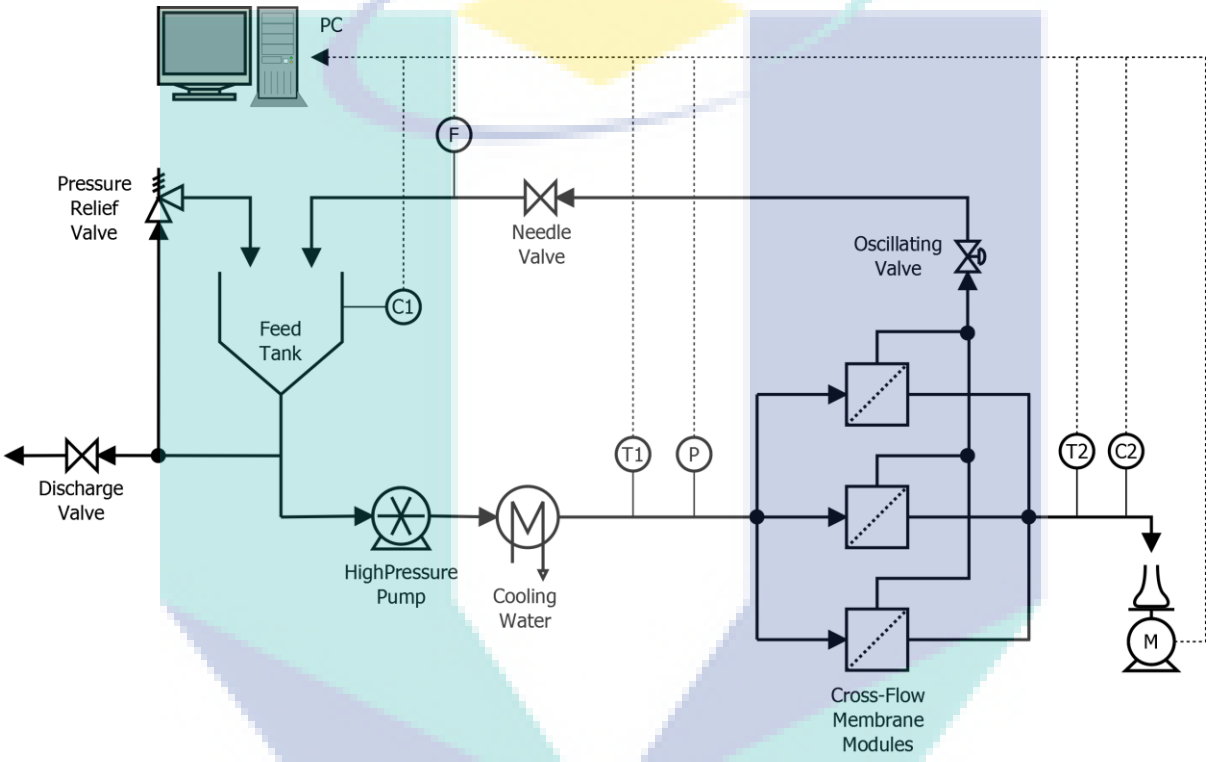

Figure 3.0.4: Piping and instrumentation diagram of the laboratory scale cross-flow system, showing pressure (P), conductivity (C), temperature (T) and mass (M) and volumetric flow (F) sensors.

Figure 3.0.5: Photograph of oscillating valve (indicated in red) and driving motor, placed on the retentate line of the RO cross-flow modules.

3.2.5 Methodology of analysis of results

The forced slip velocity CFD model used in this paper has been previously validated thoroughly against the data available in the literature [15, 18], both for steady- and unsteady-state slip velocity conditions. The permeate flux can be made dimensionless by dividing it by the pure water flux ($J_{pure} = \rho L_p \Delta p_{tm}$), given by equation (7):

$$\frac{J}{J_{pure}} = 1 - \left(\frac{\sigma \varphi R w_{b0}}{\Delta p_{tm}} \right) \gamma \tag{7}$$

The spatially local and time-averaged flux (J_{TA}), and maximum value of wall shear stress ($\hat{\tau}$) (proxy for fouling reduction [15]) are measured once the time-averaged variables have become fully developed and stabilised. Considering that the Courant number for each solution is kept below 1, the time-averaged variables usually stabilised after two residence times had passed (about 100,000 to 200,000 time steps, or around 2 weeks of wall clock time). A global or spatially average value of a local variable (ϕ) in the membrane region of length L of a unit cell (spacer 7 and 8 in Figure 3.0.1) is calculated by equation (8):

$$\bar{\phi} = \frac{1}{L} \int \phi \, dx \tag{8}$$

The maximum value of shear stress is calculated because it was reported that an increase in wall shear due to an increase in input perturbation amplitude (e.g. vibration [40]) can potentially slow down the development of membrane fouling. Wall shear stress is calculated by equation (9):

$$\bar{\tau}_{\max} = \mu \left(\overline{\frac{\partial u}{\partial y}} \right)_{\max} \tag{9}$$

In terms of energy losses, the different perturbation techniques can be compared at the same pumping power using the Power number ($Pn = Re_h^3 f_{TA}$) [16, 41]. At the same Reynolds number, an increase in Pn implies a proportional increase in pressure loss. As a white noise signal, a white Gaussian noise of zero power (dBW) time signal is generated in MATLAB and exported to the corresponding boundary condition of the CFD model as the perturbation input. The white noise input signals used for the forced-slip and oscillating flow perturbations are depicted in Figure 3.0.6a and b, respectively.

Previous work shows that stronger or more intense vortex shedding generally leads to larger pumping energy requirements [19]. In order to quantify the intensity of vortex shedding, this paper uses the λ_2 criterion [42]. Regions of vortical flow are characterised by negative values of λ_2, where a larger magnitude indicates stronger vortices.

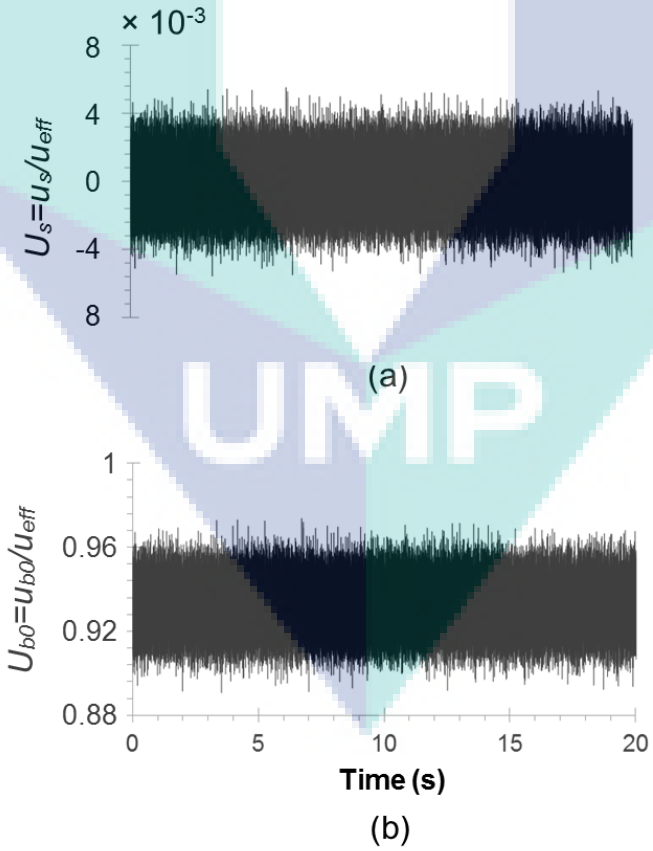

Figure 3.0.6: White noise input signal used as forced slip velocity, u_s (a) and feed flow perturbation, u_f (b)

3.3 Comparison with experimental data

Table 3.2: Comparison of numerical and experimental results for maximum flux increase under forced-transient mass transfer enhancement in a spacer-filled membrane channel, at Re = 600.

Case	Dimensionless peak frequency, F_p	Maximum flux increase (%)	Source
CFD forced-slip	0.76	21.4	[19, 38, 39]
CFD Oscillating	0.54	18.3 ± 0.7	[36, 37] and this work
Experimental Oscillating	0.48	13.5 ± 3.8	This work

Previous numerical studies of oscillating [36, 37] and forced-slip flux enhancement [19, 38, 39] have reported significant increases in permeate flux (up to about 20%). The data in Table 3. shows that a similar maximum flux increase is observed experimentally (up to about 17%) for oscillating flow at Re 600 at an F_p value in the range of 0.5–0.8. . The differences between the numerical and experimental data can be explained by the lower l_m/h_{ch} ratio used for the experiment compared with the numerical study (3.3 vs. 4), as previous numerical results [43] show that forced-slip perturbations lead to smaller flux increases when the l_m/h_{ch} ratio is decreased below 4. Therefore, this data provides support for the concept of forced-transient mass transfer and flux enhancement and for the variation in the enhancement as the perturbation frequency is changed.

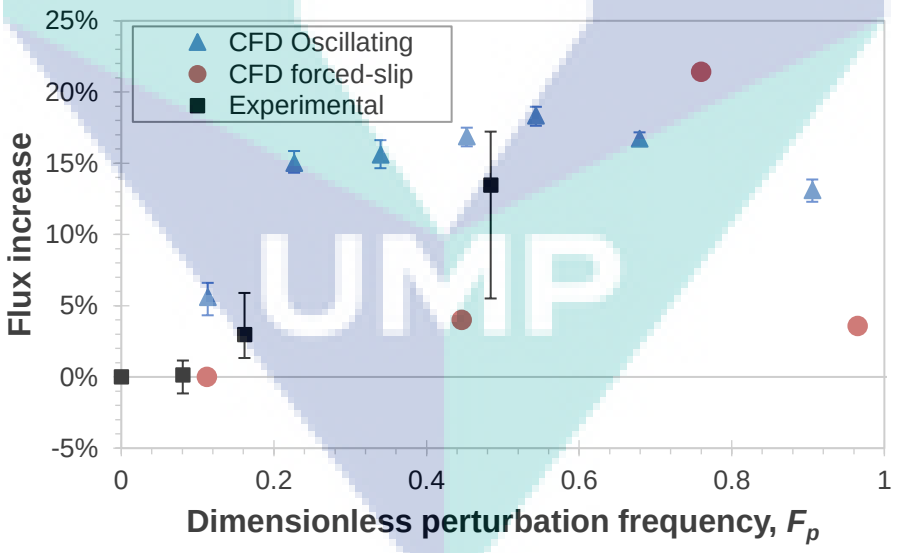

Figure 3.7: Comparison of effect of perturbation frequency on permeate flux increase for experimental and simulated oscillating flow, and simulated forced-slip perturbation, at Re = 600.

3.4 Results and Discussion

Figure 3.9 compares the performance of membrane channels under forced-slip and oscillating perturbations, against a channel without perturbations at varying values of the Power

number (*Pn*). In Figure 3.a, it can be seen that in order to achieve a similar permeate flux, the cases with forced-slip or oscillating perturbations require significantly lower Power numbers (at least 36% lower) than the case without forced transients. Figure 3.a also shows that forced-slip and oscillating flow perturbations achieve fluxes higher by at least 18%, than cases without perturbations at the same Reynolds number

In terms of the effect on fouling at the same Reynolds number, forced-slip and oscillating flow significantly increase maximum shear stress (at least 17% and up to 245%) compared to the cases without disturbance, as shown in Figure 3.b. The oscillating flow approach yields significantly higher maximum shear, but this comes at the expense of a larger Power number due to a higher pressure drop. For example, for a Reynolds number of 400, forced slip increases the maximum shear by about 49% at the expense of 1.5% higher pressure drop compared to the case without perturbation, whereas the oscillating feed increases maximum shear by around 245%, but pressure drop increases by 15%.

The pressure drop analysis agrees with the results for λ_2 shown in Figure 3.9, which shows that the shed vortices are stronger for oscillating flow than for forced slip, leading to greater form drag (hence a larger fanning friction factor) and stronger wall scouring (hence larger wall shear), both of which lead to increased pressure losses. This is because wall shear and form drag are both fluid energy sinks, by means of which the mechanical energy of the fluid (pressure) is dissipated and converted to thermal energy. Hence, oscillating the bulk flow requires more pumping energy because much of this extra energy input is required to change the momentum of a larger volume of fluid (evidenced by stronger vortices), rather than to only disrupting the boundary layer as is done in the forced-slip approach. The extra pumping energy requirement is dissipated as wall shear and form drag, which can be corroborated by the higher increase in wall shear for oscillating flow compared to forced slip (see Figure 3.).

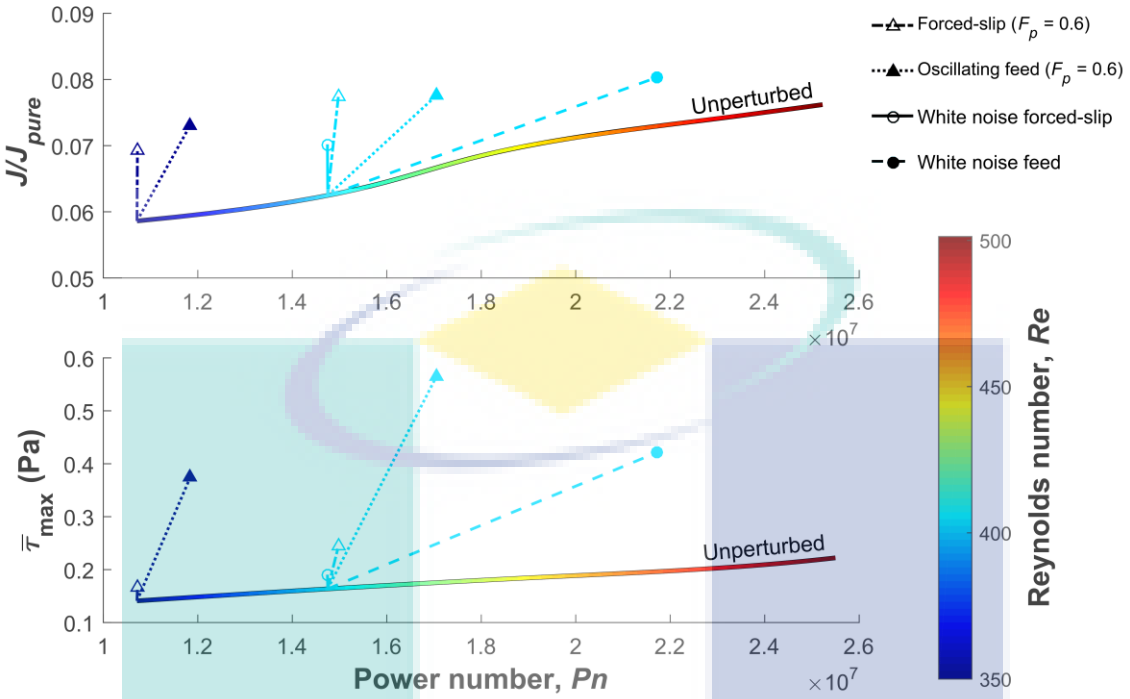

Figure 3.8: Effect of *Pn* with and without input perturbation on (a) dimensionless permeate flux (b) Maximum shear stress. The dotted lines indicate the change at constant Reynolds number due to a type of perturbation.

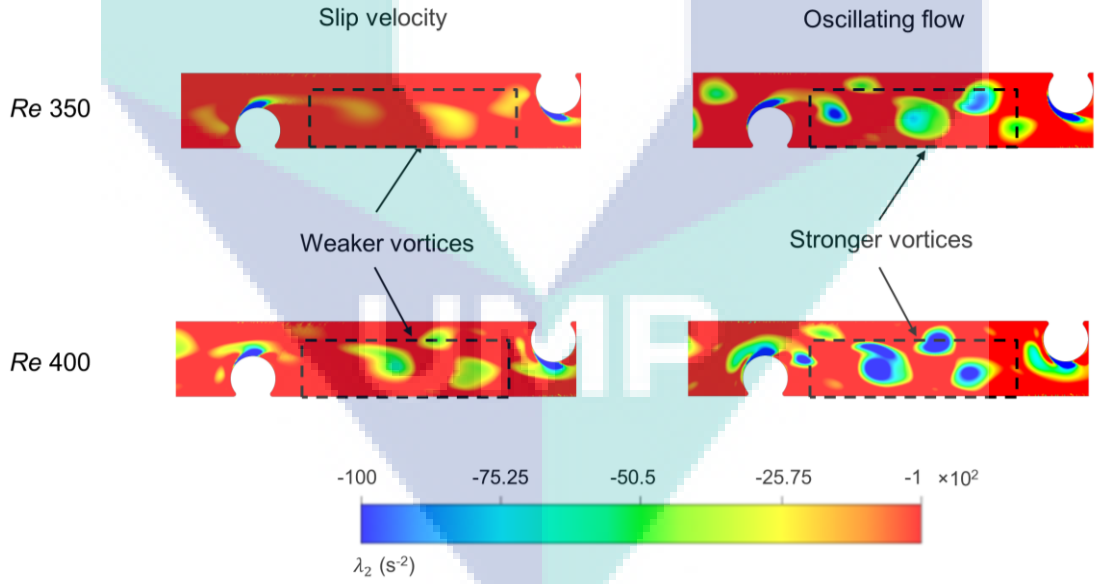

Figure 3.9: Effect slip velocity and oscillating flow on the magnitude of λ_2 at *Re* 350 and 400.

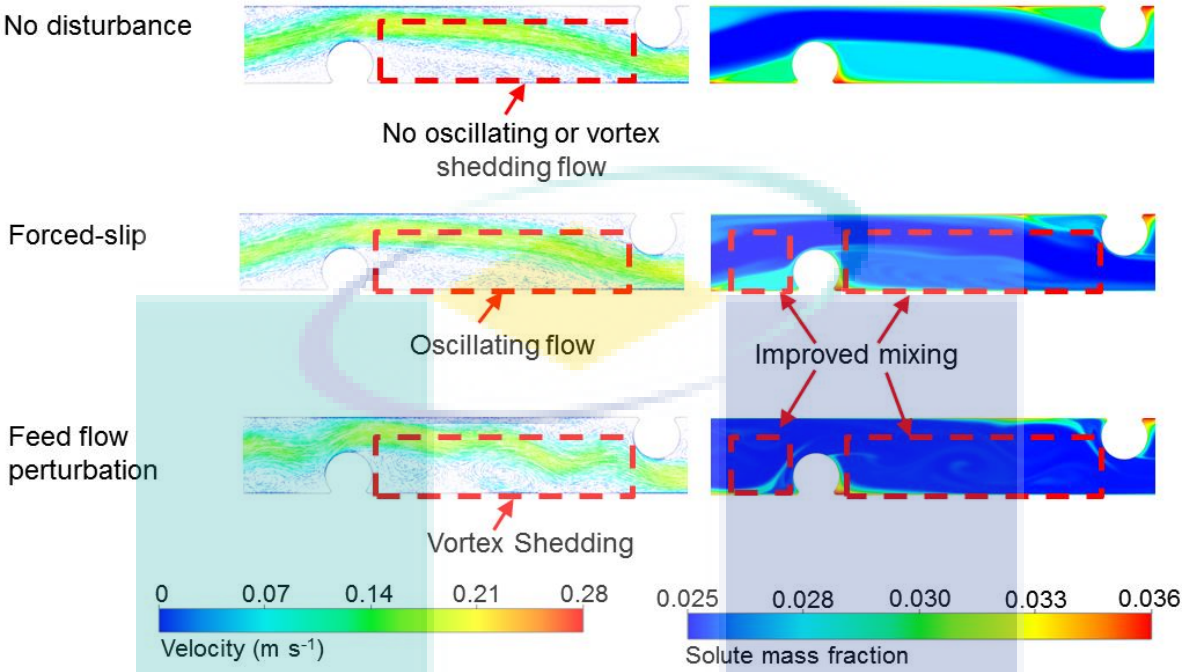

Figure 3.10: Effect of single frequency oscillating or forced-slip perturbations at 14 Hz (F_p = 0.6), on the velocity field and solute concentration for *Re*=350.

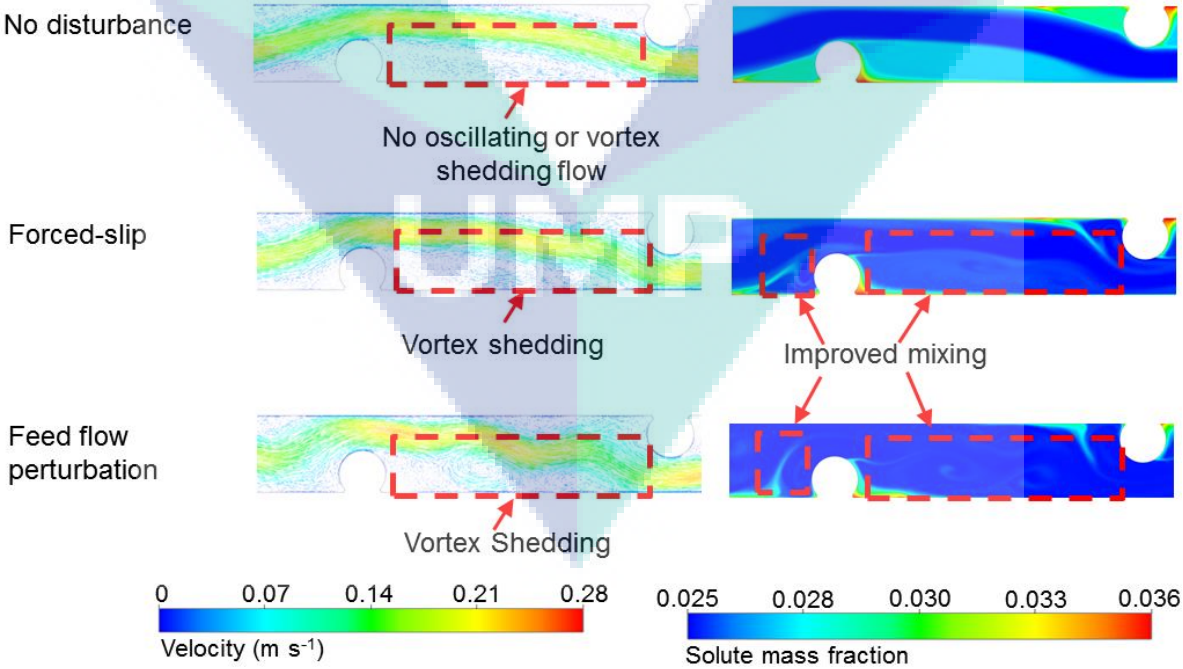

Figure 3.11: Effect of single frequency oscillating or forced-slip perturbations at 16 Hz (F_p = 0.6), on the velocity field and solute concentration for *Re*=400.

Given that both oscillating and forced-slip perturbations show similar magnitude of increases in terms of permeate flux, this suggests that the mechanism by which the flow perturbations are generated is not as important as the frequency of the disturbance applied. The results shown in **Error! Reference source not found.** and Figure 3. reinforce this finding. Under steady flow, recirculation regions form upstream and downstream of each filament, and mass transfer in or out of these regions (in the direction of the boundary layer) occurs via diffusion only because the streamlines within the recirculation regions are close loops [5]. On the other hand, when there is oscillating flow or vortex shedding, the streamlines are not closed and the upstream recirculation regions draw low solute concentration fluid towards their vortex core, reducing the concentration closer to the filament and the membrane surface, which in turns improves mass transfer [28]. This effect is also evident for the downstream recirculation regions for both types of perturbations. The larger flux increase shown in Figure 3. for the oscillating feed can be related to the onset of vortex shedding, which is absent for the forced-slip case at Re 350 (**Error! Reference source not found.**10). On the other hand, for Re 400 (Figure 3.) both the oscillating feed and forced-slop cases show vortex shedding, resulting in similar flux increases.

White noise perturbations are also studied to determine if they can induce boundary layer renewal in membrane channels. This effect is confirmed in Figure 3., where it can be seen that forced-slip and feed flow perturbations induce transient (periodic) flow and vortex shedding, respectively. It is interesting to note that only the oscillating perturbations produced vortex shedding. This is because, as shown in Figure 3.0.6, the velocity variations induced by feed flow perturbations are about one order of magnitude larger than those for the case using forced-slip approach. Therefore, feed flow perturbations result in more mixing than forced-slip perturbations. Nonetheless, the white noise feed perturbation requires a significantly higher pumping energy (at least 27% higher) than any single-sinusoidal flow perturbation approach.

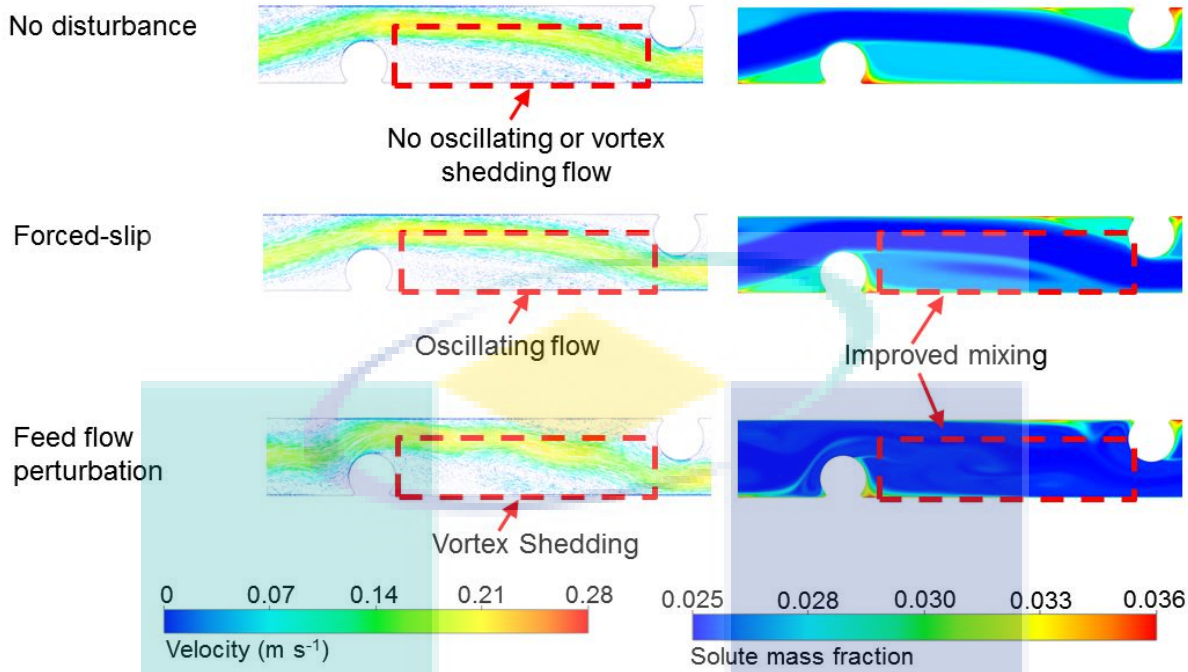

Figure 3.12: Effect of white noise feed and forced-slip perturbations on velocity field and solute concentration for *Re* 400.

The occurrence of periodic flow induced by forced-slip perturbations, suggested by Figure 3.12 and shown in Figure 3., indicates that the flow tends to oscillate at a preferred frequency rather than oscillating at every frequency component in the white noise. Figure 3. shows that the flow velocity oscillates at particular frequency under both feed and slip perturbations, F_p ~0.67 (obtained from the Fourier transform of *v*-velocity). Interestingly, the frequency observed for the flow under white noise feed flow perturbations at which vortex shedding occurs (F_p = 0.62) is very close to the peak frequency (F_p = 0.6) for sinusoidal oscillating flow found in a previous study at the same *Re* [36]. This also agrees with our previous findings [39], that the flow tends to react to the peak/resonant frequency regardless of the waveform of the input perturbation. Hence, the use of white noise as an input perturbation simplifies the approach for inducing periodic flow in membrane channels, as the peak or resonant frequency does need to be identified *a-priori*. However, using white noise increases the perturbation energy input because energy needs to be supplied over a wider spectrum of frequencies. In addition, white noise is less effective at increasing wall shear than single frequency perturbations (see Figure 3.8) and can be cumbersome to implement mechanically for feed flow perturbations.

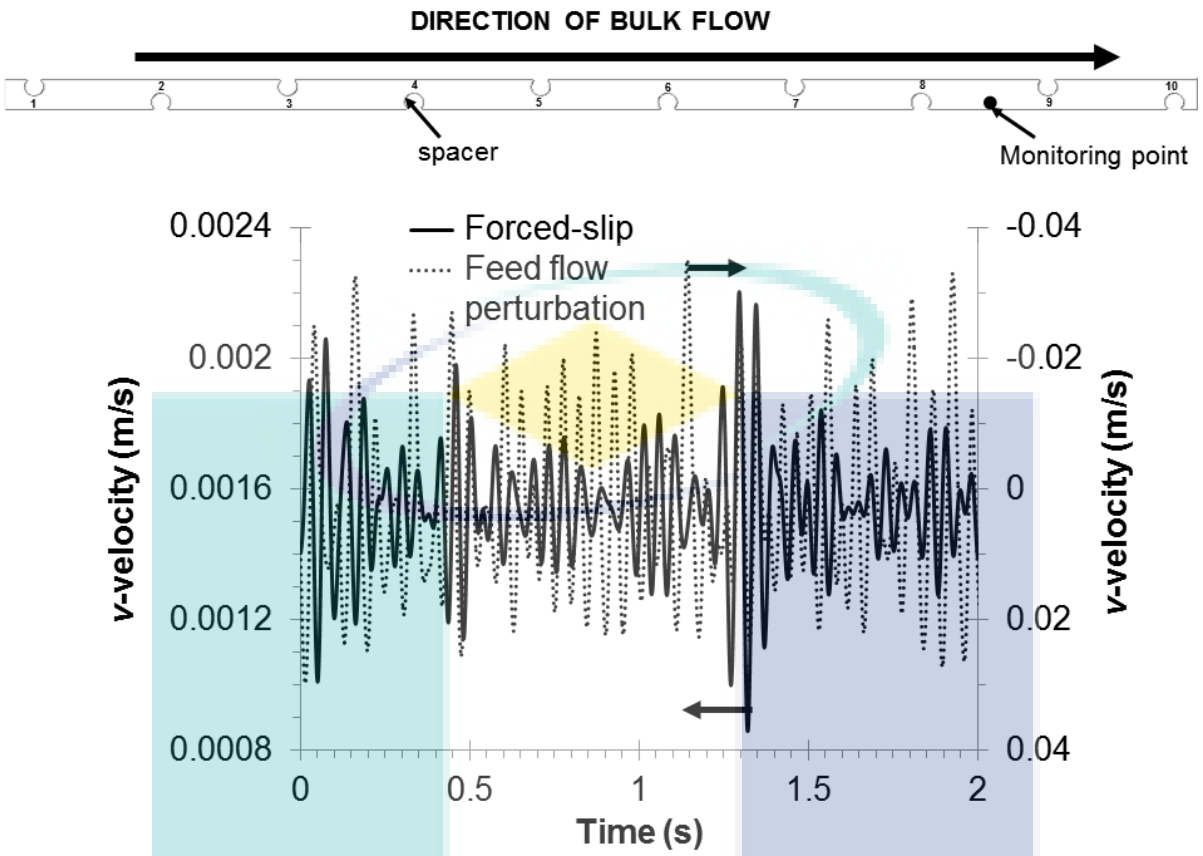

Figure 3.13: Effect of white noise feed flow perturbation and forced slip velocity on *v*-velocity at monitoring point '•' (located at one quarter of the channel height from the bottom membrane surface) for *Re* 400.

3.5 Conclusion

The effect of forced-slip perturbations in 2D spacer-filled RO membrane channels is compared to the effect of oscillating feed perturbations at the same peak/resonant frequency and Reynolds number, in terms of wall shear and mass transfer. It was found that both approaches show similar magnitude increases in permeate flux (more than 17%) and a similar flow regime in the channel. These results imply that the mechanism by which the flow perturbations are generated is not as crucial as the perturbation frequency used, as small oscillations are naturally amplified by the channel, eventually leading to vortex shedding and mass transfer enhancement.

The results presented in this paper suggest that if the channel peak/resonant frequency is known, applying the perturbations near the concentration boundary layer is more energy efficient than oscillating the bulk flow. This is because less energy is required to change the momentum of the smaller volume of fluid within the thin boundary layer. The data presented in this paper also confirm that white noise perturbations can be used to induce boundary layer renewal and vortex shedding without the need to identify the peak/resonant frequency *a-priori*.

The occurrence of vortex shedding when applying white noise perturbations suggests that the membrane channel tends to promote the amplification of specific frequency oscillations, even though the white noise input contains many other frequencies with equal intensity. However, using white noise for perturbing the feed flow requires significantly more pumping energy than any single-sinusoidal flow perturbation approach. This implies that most of the energy in white noise perturbations is dissipated in the channel and hence wasted, because only a single frequency is important for enhancing mass transfer.

It is worth noting that the simulations used for this study were carried out in 2D flow, which does not account for the flow patterns (e.g. vortex stretching) and associated wall shear and other mass transfer enhancement mechanisms present in 3D flow. As analysing 3D flow results will give more insights into mass transfer enhancement mechanisms than 2D flow studies, future works to investigate these 3D effects under unsteady disturbances are recommended, particularly for varying geometric parameters.

Acknowledgements

The authors acknowledge the Sydney Informatics Hub and the University of Sydney's high performance computing cluster Artemis for providing the high performance computing resources that have contributed to the research results reported within this paper. Funding support by Universiti Malaysia Pahang research grants (Project numbers RDU160342, RDU170324 and PGRS170341), CONACYT (PDCPN 2015-1221 and Cátedras Project 2338) and by the Instituto Tecnológico de Sonora (PROFAPI fund Project 2018-0029) is also acknowledged. Thanks are extended to Ismael Murillo Verduzco for assisting with the fabrication of the oscillating valve, and to José Luis Robles Magdaleno for support in obtaining the experimental data.

CHAPTER 4

CFD study of the effect of SWM feed spacer geometry on mass transfer enhancement driven by forced transient slip velocity

K. Foo[a], *Y. Y. Liang*[a,b*], *G. A. Fimbres Weihs*[c,d]

[a]Faculty of Chemical and Natural Resources Engineering, Universiti Malaysia Pahang Lebuhraya Tun Razak, 26300 Gambang, Kuantan, Pahang, Malaysia
[b]Centre of Excellence for Advanced Research in Fluid Flow (CARIFF), Universiti Malaysia Pahang, Lebuhraya Tun Razak, 26300 Gambang, Kuantan, Pahang, Malaysia
[c]CONACYT–Instituto Tecnológico de Sonora, 5 de Febrero 818 Sur, Cd. Obregón, Sonora, C.P. 85000, México
[d]School of Chemical and Biomolecular Engineering, The University of Sydney, NSW 2006, Australia

[*] Corresponding author. Tel.: +609 549 2859. E-mail: yongyeow.liang@ump.edu.my

Abstract

Recent studies have shown that the interactions between forced transient flow and eddy inducers (i.e. spacers) in spiral wound membrane modules results in significant mass transfer enhancement and reduction in concentration polarisation (CP). This paper uses CFD to investigate the effect of varying the spacer geometric parameters on the resonant frequency for an unsteady forced-slip, as well as the resulting permeate flux enhancement, for a 2D zig-zag spacer. The analysis shows that the resonant frequency is significantly affected by the interaction of the shear layer with successive downstream spacers. The effectiveness of forced-slip reaches a peak (up to 15.6% flux increase) for a spacer size in the range of $0.5<d_f/h_{ch}<0.6$ because of the trade-off between mixing-induced forced-slip and the CP modulus. In addition, vortex shedding is suppressed for smaller spacer sizes ($d_f/h_{ch}\leq0.4$), because viscous forces dominate over convective forces due to a smaller filament Reynolds number. As the distance between filaments is increased, the increase in flux due to forced-slip is greater (up to 31.5%), albeit the actual flux decreases because the boundary layer is more developed. These results also reinforce the finding that forced-slip is more efficient for spacer designs with poor mixing (i.e. high CP).

Keywords:

CFD, unsteady slip velocity, spacer geometry, mass transfer enhancement

4.1 Introduction

Spiral wound membrane (SWM) modules are a basic component for reverse osmosis (RO) desalination and other membrane based water treatment applications, because they offer a good balance between permeation rate, pressure loss and fouling control [44]. A major problem in SWM modules is concentration polarisation (CP), a phenomenon characterised by solute accumulation near the membrane surface due to membrane rejection [45, 46]. Spacers in SWM modules not only function to separate membrane leaves, but also to enhance mixing and ultimately to reduce CP.

It is known that spacers can be modified to help promote the unsteadiness of flow inside spacer-filled channels, leading to increased boundary layer renewal [47] and improving solute mass transfer. This is because spacer orientation and geometric parameters have a significant effect on the hydrodynamics inside spacer-filled channels [48, 49]. For example, Schwinge et al. [50] show that for a constant channel height (h_{ch}), there is a maximum in mass transfer enhancement when varying the mesh length (l_m) of zig-zag and cavity configurations, and pressure losses increases as the mesh length decreases. They also reported that a smaller ratio of filament diameter to channel height (d_f/h_{ch}) is preferable over a larger spacer, as it increases mass transfer relative to pressure loss [50]. On the other hand, Park et al. [8] found that a thicker feed spacer (larger d_f) may be effective in reducing fouling, because it provides a wider space between the membrane surface and feed spacer. The larger space was observed to lead to a reduced rate of precipitation of foulants on the membrane surface, as well as a more homogeneous distribution of foulants in the RO elements [51].

Guillen et al. [6] suggested that the spacer geometry has a stronger effect on pressure losses than on mass transfer. Nonetheless, pressure losses inside spacer-filled channels are dependent on both the flow regime (viz. steady or unsteady) and the spacer dimensions. For example, Alexiadis et al. [9] found that the friction factor (a dimensionless pressure loss metric) increases significantly when the flow regime in spacer-filled membrane channels changes from steady-state to unsteady flow patterns. In addition, a larger spacer diameter or a reduced mesh length decrease the critical value of the Reynolds number (Re_{CR}) at which improved mixing due to transient flow can be attained without excessive pressure loss [52]. A smaller spacer diameter or a larger mesh length, conversely, lead to larger values of Re_{CR}.

In addition to efforts to increase mass transfer by modifying the spacer geometry [49, 50, 52-55], there are also other approaches that can be used to enhance mixing. These latter approaches attempt to induce or force transient (unsteady) flow by means of hydrodynamic

perturbations, such as vibrations, pulsatile/oscillating flow, and electro-osmotic flow (EOF) slip velocity. A few studies have also combined spacer modifications with unsteady flow perturbations to improve membrane performance [19, 20, 56]. For example, Su et al. [57] found that the CP modulus decreases as the frequency of vibration increases. They also found that a higher frequency of forced vibrations induces more vortex shedding than cases without vibration, and that induced vortex shedding eventually improves the wall shear rate and enhances mass transfer. However, the increase in boundary shear rate caused by membrane vibration is less effective for systems with larger Reynolds number (*Re*) than for lower *Re* [57]. These findings agree with the work of Liang et al. [19] using forced-slip to induce transient flow, which showed that imposed flow perturbations have less impact on a system which is already well mixed (e.g. at a higher Reynolds number).

Forced-slip is the motion of the fluid adjacent to the membrane surface, relative to the surface, which may result from applied electric (e.g. electro-osmosis) or mechanical force (e.g. vibration). Because forced-slip directly disturbs the concentration polarisation layer near the membrane, it has potential to effectively enhance mass transfer and permeate flux. Previous studies of mass transfer enhancement in spacer-filled membrane channels [38, 39, 57, 58] have suggested that forcing transient flow near the membrane surface can be achieved by any source of hydrodynamic perturbation (e.g. vibration, slip velocity, oscillating flow). Some studies [39, 57] have also reported a similar magnitude of flux enhancement (~10–20%) inside spacer-filled channels, regardless of the source or waveform of the perturbation.

Moreover, the importance of applying perturbations at the resonant frequency (or peak frequency) for maximising their effect, has been highlighted [19, 37]. However, those studies have only considered a single spacer geometry under forced-slip, so there is a lack of understanding of how the spacer geometric factors influence the mechanism that leads to increased flux. This is because the spacer geometry affects both the degree of mixing and the natural frequencies of the flow inside the spacer-filled channel. Hence, the resonant frequency (and thus the frequency of boundary layer renewal) is expected to vary for different spacer geometries.

This paper aims to use computational fluid dynamics (CFD) to examine the effect of spacer geometry on the resonant frequency of forced-slip, as well as the resulting increases in shear stress. The study uses the forced-slip model employed in previous works [18, 19, 59]. Although those studies are purely numerical in nature, the model has been validated against data available from the literature, under steady [18] and unsteady [59] conditions. Thus, this

gives confidence in the present work, which uses the CFD model to identify the spacer geometry at which forced-slip velocity perform best in terms of mass transfer enhancement. The spacer geometries considered in this study are the simple 2D zig-zag spacer configurations with variations in diameter and mesh length typically used for membrane RO systems [18]. All spacer geometries under forced-slip are compared in terms of flux, wall shear and energy loss at the same hydraulic Reynolds number (Re_h).

4.2 Methodology

4.2.1 Model description

The commercial CFD software (ANSYS CFX 18.2) is adopted in this paper to simulate two-dimensional (2D) Newtonian fluid inside a narrow spacer-filled membrane channel. Constant fluid properties are employed, and negligible gravitational effects are assumed [50, 59]. The governing Navier–Stokes and mass transfer equations are therefore as follows:

$$\nabla \bullet \vec{v} = 0 \tag{10}$$

$$\rho \frac{\partial \vec{v}}{\partial t} + \rho \left(\vec{v} \bullet \nabla \right) \vec{v} = \mu \nabla \bullet \left(\nabla \vec{v} + \nabla \vec{v}^{T} \right) - \nabla p \tag{11}$$

$$\rho \frac{\partial w}{\partial t} + \rho \nabla \bullet \left(w \vec{v} \right) = \rho D \nabla^{2} w \tag{12}$$

The simulations in this paper assume 2D flow. This is because the computational resources and time required for 3D simulations are much larger than 2D simulations [60]. Most importantly, it has been reported that there are no notable 3D effects for the Reynolds number considered in this paper ($Re_h = 425$) [61, 62]. Therefore, 3D effects are not expected to change the trends in hydrodynamics and permeate flux reported in this paper. The zig-zag spacer configuration (Figure 4.0.1) is chosen as case study because it has been shown to lead to better mass transfer and pressure drop performance than other 2D geometries (i.e. submerged, cavity) [48, 50].

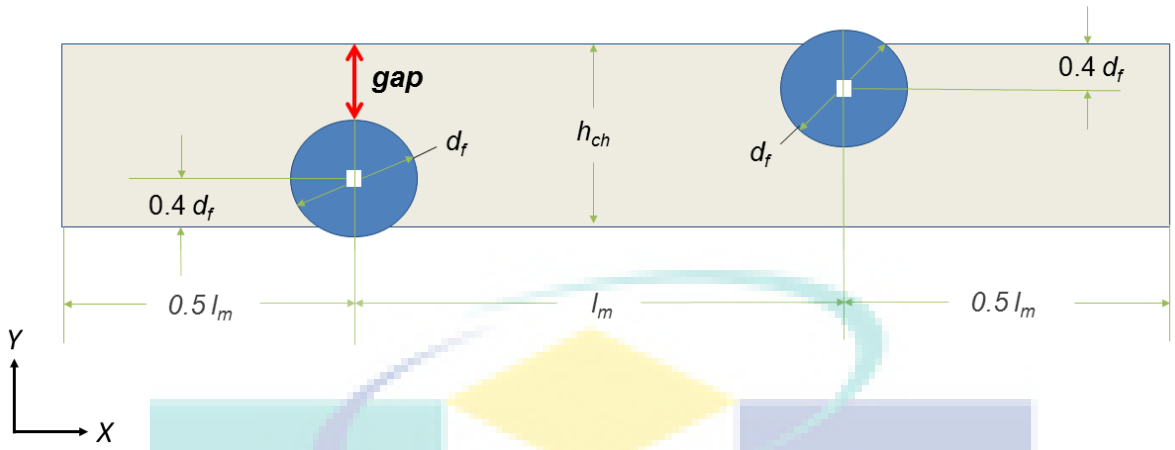

Figure 4.0.1: Geometry of the zig-zag spacer unit cell. The red arrow indicates the gap between the spacer filament and the membrane surface where the flow velocity is measured.

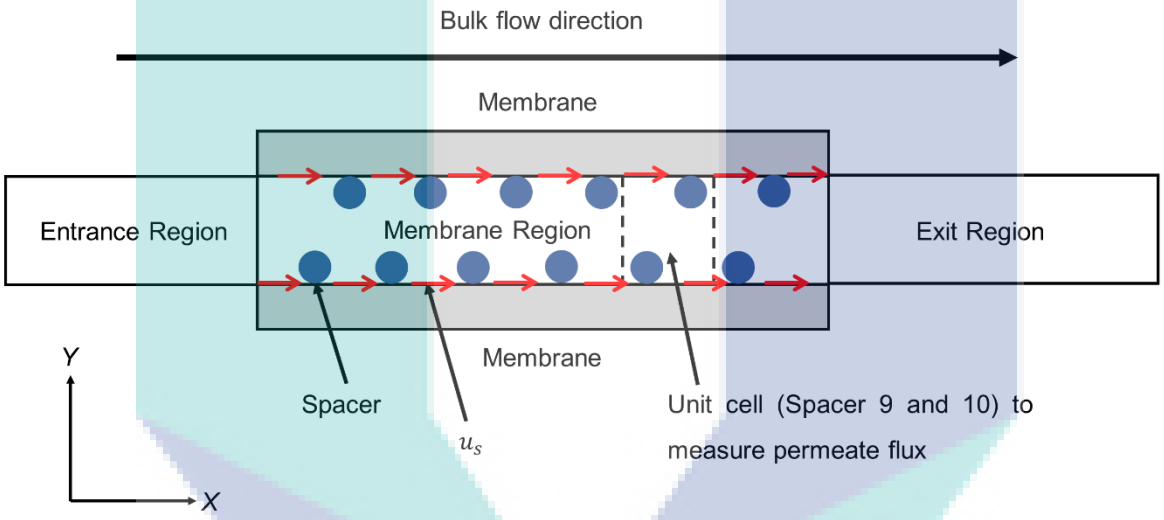

Figure 4.0.2: Schematic diagram of the fluid domain (not to scale) showing the boundary conditions and membrane channel regions, with red arrows on the membrane surface representing the location of forced-slip.

Based on previous work, both by the authors and by other researchers [48, 50, 53, 63, 64], the length of the entrance region used in this study is set as 20 times the spacer diameter (d_f), and the exit region as twice of the length of the entrance region, in order to ensure the flow solution is not affected by the inlet and outlet boundary conditions. The fluid domain includes 12 spacers (Figure 4.0.2), as the flow is reported to become fully developed after only about five or six spacers [63, 64]. All the detailed analysis of friction and mass transfer parameters performed on the fifth unit cell (9th and 10th spacer filaments). In order to keep a constant hydraulic Reynolds number (Re_h) of 425, the same values of hydraulic diameter (d_h) and effective flow velocity (u_{eff}) are used for all spacer geometries under consideration, but the membrane channel height (h_{ch}) and volumetric feed flow rate are varied accordingly.

4.2.2 Boundary conditions

As mentioned in the Introduction, there are several methods to induce forced-slip, namely vibration [20, 57] and electro-osmosis [18, 19, 59]. The forced-slip model used in this paper follows the Helmholtz-Smoluchowski (HS) approximation for modelling electro-osmotic flow [18, 59]. The HS slip velocity (u_s) approximation is given by:

$$u_s = -\frac{\varepsilon_e \zeta E_x}{\mu} \tag{13}$$

where ε_e, ζ, E_x and μ are permittivity, zeta potential, electric field in the x-direction and dynamic viscosity, respectively.

A dimensionless measure of the HS slip velocity can be defined by using the hydraulic diameter and fluid properties (i.e. viscosity and density), referred to as the slip Reynolds number ($Re_s = \rho u_s d_h/\mu$). The transient forced-slip is modelled as a single-frequency sinusoidal slip velocity as follows:

$$U_{s,t} = \frac{u_{s,A}}{u_{eff}} \sin\left(2\pi f_s t\right) = U_{s,A} \sin\left(2\pi f_s t\right) \tag{14}$$

where t, f_s, u_{eff} and $u_{s,A}$ are time, frequency of oscillation, effective velocity and slip velocity amplitude, respectively.

According to the Kedem–Katchalsky model [65], the permeate volumetric flux across the membrane region (v_w) can be calculated as a function of local salt concentration on the membrane surface:

$$v_w = \frac{J}{\rho} = L_p \left(\Delta p_{tm} - \sigma \varphi R w_w\right) \tag{15}$$

where J, ρ, L_p, Δp_{tm}, σ, φ, R and w_w are permeate flux, fluid density, membrane permeance, inlet transmembrane pressure, reflection coefficient, osmotic pressure coefficient, membrane intrinsic rejection and solute mass fraction on the feed side membrane surface, respectively.

The solute mass fraction at the membrane surface is determined by the CFD model based on the mass-flux balance calculation, which acts as the concentration boundary condition on the membrane [18]:

$$\left(\frac{\partial w}{\partial y}\right)_w = -\frac{J R w_w}{\rho D} \tag{16}$$

where D is solute diffusivity.

Other solid domain boundaries (i.e. spacer surfaces, entrance and exit region channel walls) are specified as no-slip boundary conditions with zero mass flux ($\partial w/\partial n = 0$). At the inlet, a parabolic velocity profile as in equation (8) is specified, whereas a zero average reference pressure is specified at the outlet boundary.

$$u_{b0} = 6u_{avg}\frac{y}{h_{ch}}\left(1-\frac{y}{h_{ch}}\right) \tag{17}$$

where u_{b0}, u_{avg}, y and h_{ch} are the inlet velocity profile, average velocity, distance from the bottom membrane surface in direction normal to the surface, and channel height, respectively.

4.2.3 Assumption and cases

By means of a mesh independence study, grid convergence indices (GCI) below 5% were obtained for both permeate flux and friction factor. This means that potential sources of numerical error due to insufficiently fine meshing can be safely neglected. The fluid domain was discretised using at least 2.5 million control volumes (for the shortest channel), and at most of 6.4 million control volumes for the case with the largest mesh length (l_m/h_{ch} = 10). To properly resolve the velocity and concentration boundary layers (where the gradients are the largest), the discretised domain consists of at least 30 control volumes within all surface boundary layers (approximately 2% thickness of membrane channel height).

Taking into account that the Courant number for each solution is kept below 1, all the simulations conducted required more than 100,000 time steps, or around 3 to 4 weeks of wall clock time to achieve convergence for the hydrodynamics and mass transfer. In terms of computational time and memory, the simulations required more than 100 h of computational times and at least 11 GB of memory on 6-core and 8-core Xeon Processors running at 3.7 GHz and 3.2 GHz, respectively.

The detailed dimensionless parameters and variable ranges for the forced-slip case studies are shown in Table 4.1. In the simulations, the dimensional values of the hydraulic diameter and effective velocity are set as constant at 1.66×10^{-3} m and 0.26 m/s, respectively, and the remaining dimensions (h_{ch}, d_f, slip velocity, etc.) are calculated from the Reynolds number and other dimensionless parameters. Although the parameters used in this paper are dimensionless, it is possible to obtain dimensional results by using the definition of the dimensionless numbers. Due to the dimensionless nature of the Navier-Stokes equations, this implies that the solutions presented will be self-similar as long as the dimensionless quantities remain the same.

Table 4.1: Parameters used for forced-slip case studies.

Parameter	Value
Feed solute mass fraction (w_{b0})	0.025
Dimensionless spacer diameter (d_f / h_{ch})	0.4–0.7
Dimensionless mesh length (l_m / h_{ch})	3–10
Dimensionless inlet transmembrane pressure ($P_0 = \Delta p_{tm} / \pi_0$)	1.46
Dimensionless forced-slip velocity amplitude ($U_{s,A} = u_{s,A} / u_{eff}$)	1.96×10^{-3}
Intrinsic rejection (R)	0.996
Dimensionless membrane permeance ($\boldsymbol{\Pi}_{\boldsymbol{L_p}} = L_p\ \pi_0 / u_{eff}$)	3.06×10^{-4}
Reflection coefficient (σ)	1
Hydraulic Reynolds number ($Re_h = \rho\, u_{eff}\, d_h / \mu$)	425
Slip Reynolds number ($Re_s = \rho\, u_{s,A}\, d_h / \mu$)	0.83

4.2.4 Methodology for analysis of results

The transient simulations are considered to have converged once the time-averaged (ϕ_{TA}) and maximum (ϕ_{max}) values of spatially local variables have stabilised. When those conditions are met, the global variables ($\bar{\phi}$) (i.e. permeate flux, wall shear) are calculated as the area-average of the local variables within the membrane region length (L) for a unit cell (as indicated in Figure 4.0.1) as follows:

$$\bar{\phi} = \frac{1}{L}\int \phi dx \tag{18}$$

For comparing the potential for long-term fouling reduction by the different spacer geometries, maximum wall shear stress ($\bar{\tau}_{\max}$) is used as a proxy measure. This is because a larger value of shear rate results in a larger potential for reducing the tendency for membrane fouling [39]. The maximum wall shear stress is defined as:

$$\bar{\tau}_{\max} = \mu\left(\frac{\overline{\partial u}}{\partial y}\right)_{\max} \tag{19}$$

In terms of energy consumption, the Power number ($Pn = Re^3 f_{TA}$) is used to compare energy losses for different spacer geometries. Under the assumption of the same values for hydraulic diameter, effective velocity and Reynolds number, the pumping energy (and hence the Power number) is directly proportional to pressure per unit length ($\Delta p/L$) for all spacer geometries under consideration.

In order to identify the peak frequency of forced-slip for a given spacer geometry, a frequency response analysis is used in this study. The frequency response is a plot of the

amplitude ratio of an observed output for a given input stimulus, as a function of the input frequency. The amplitude ratio is calculated by dividing the Fourier transform of the output by the Fourier transform of the input. The frequency at which the maximum amplitude ratio is observed is termed the peak frequency (f_{pl}). It is important to note that the frequency response analysis is ideally to be used for a system that exhibits a linear input-output relationship [66]. Nonetheless, frequency response analysis can be used to approximate f_{pl} for a mildly non-linear system [67].

Following our previous study [67], a frequency response test is carried out using a pulse in the slip velocity ($u_{s,pulse}$) as input applied everywhere along the top and bottom membrane surfaces with a cut-off frequency (f_{cut}) value of 500 Hz. A large $u_{s,pulse}$ value of 0.001 m/s is used, which corresponds to twice as large as the amplitude of the sinusoidal slip velocity ($u_{s,A}$). This larger value is used in order to increase the sensitivity of the test and facilitate the determination of the response spectra. Further, the magnitude of flow perturbation is not as important as the frequency [58]. In addition, the magnitude of the pulse only affects the amplitude in the early membrane channel, but not for the following unit cells because the natural frequency is amplified and the oscillations grow naturally. Thus, this means that increasing the amplitude of the pulse only moves the point of vortex shedding towards the inlet but does not affect the peak frequency. Thus, the insights from this test are still applicable because the larger slip velocity is only used to obtain the frequency response without having to resort to a longer simulation time or a longer membrane channel, which would require more computational resources.

The pulse in slip velocity is given by:

$$u_{s,pulse} = \frac{U_{s,A}}{2}\left[1-\cos\left(\frac{2\pi t}{t_{fcut}}\right)\right] \tag{20}$$

where

$$t_{fcut} = \frac{4}{\pi f_{cut}} \tag{21}$$

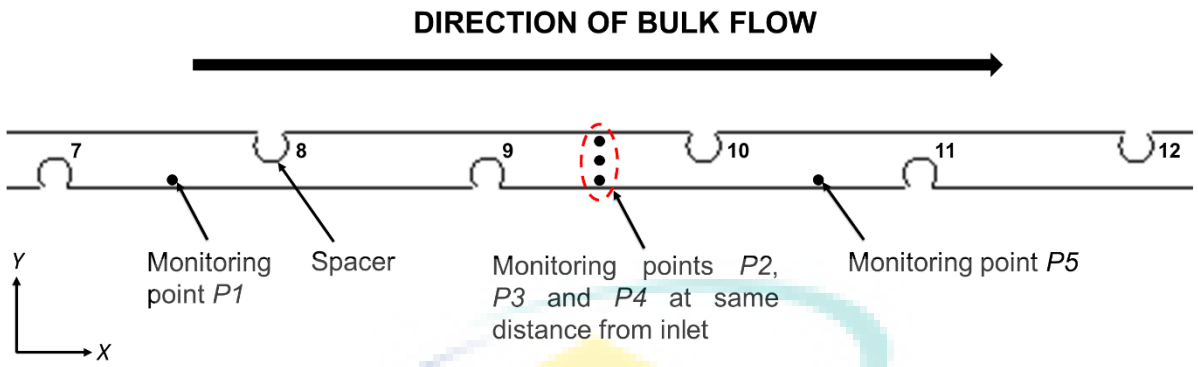

Figure 4.0.3: Schematic of the location along the membrane channel of the monitoring points '•' used for the frequency response tests. P1 and P5 refer to monitoring points located at 10% of the channel height from the bottom membrane surface for the unit cell comprised of the 7th and 8th spacers, and 10th and 11th spacers, respectively. P2, P3 and P4 refer to monitoring points located at 10%, 50%, and 90% of the channel height at the same distance from the inlet for the unit cell comprised of the 9th and 10th spacers.

An upper limit of 500 Hz for the value of f_{cut} is used, as it was found that it is sufficiently high to identify the frequency with the largest amplitude ratio for the fluid flow domain in question. The response is taken to be the v-velocity at the monitoring points (indicated by the black dots in Figure 4.0.3). During the pulse test, vortices are shed as they detach from upstream spacer, which leads to oscillations in v-velocity at the monitoring points.

From the frequency response analysis, f_{pl} is determined and used for the simulations of single-frequency sinusoidal slip-velocity (f_s) for all the geometric cases considered. As it has been observed that the peak frequency corresponds to the vortex shedding frequency [39], f_{pl} can be expressed as the dimensionless Strouhal number (St) using the spacer diameter (d_f) as the length scale and the average fluid u-velocity measured at the gap between the membrane surface and spacer ($\bar{u}_{gap}$, as shown in Figure 4.0.2) as the velocity scale [63]. Thus, the Strouhal number is given by:

$$St = \frac{f_s d_f}{\bar{u}_{gap}} \tag{22}$$

where

$$\bar{u}_{gap} = \frac{u_{b0} h_{ch}}{h_{gap}} \tag{23}$$

The Strouhal number is also a measure of the ratio of transient flow forces to inertial forces associated with the mean velocity at the gap between the membrane surface and the spacer ($\bar{u}_{gap}$). The value for $\bar{u}_{gap}$ is measured based on the inlet velocity (u_{b0}) rather than at any location within the membrane region as it was found that its value is not significantly

affected by permeation in the short channel under consideration. For cylindrical structures, the *St* is typically around 0.2, which indicates the occurrence of rapid vortex shedding in the flow system [68]. Because the occurrence of vortex shedding is dependent on the resonant frequency [19], it can be interpreted that a higher Strouhal number results in a larger frequency of boundary layer renewal, which thus improves mass transfer.

It has been shown elsewhere [19, 48] that the shedding of vortices adjacent to the membrane surface plays an important role in membrane mass transfer enhancement. There are two popular vortex identification methods, namely the Q and λ_2 criteria [69]. The λ_2 criterion is particularly suitable for flows with low Reynolds number and unsteady flow regime [42], whereas the Q-criterion is more suitable for turbulent flow [69]. Because the typical Reynolds numbers used in membrane systems are usually of the order of 100 [70], λ_2 is a preferable criterion to be used for identifying vortices. It should be noted that the existence of vortex cores can only be shown by the negative value of λ_2; thus, a larger magnitude of the negative value of λ_2 indicates a stronger vortex.

4.3 Results and discussion

An example of frequency response pulse test for $d_f/h_{ch} = 0.6$ and $l_m/h_{ch} = 4$ is shown in Figure 4.. It can be seen that the *v*-velocity oscillates in response to pulse input and then the oscillations dissipate as time progresses, due to viscous effects [59]. The results in Figure 4.5 indicate that the location of monitoring point does not have a significant effect on the frequency response, because the peak frequency (the one with the largest amplitude) is similar regardless of the monitoring point selected. For example, the data measured at 3 points at different locations at the same channel height as the monitoring locations (as indicated in Figure 4.) shows that the peak frequency is similar regardless of the monitoring point. In addition, the peak frequency is similar for the unit cell comprised of the 7^{th} and 8^{th} spacers, and 10^{th} and 11^{th} spacers, respectively. This is because the flow in a spacer-filled membrane channel usually becomes fully developed after five to six spacer filaments [63, 64]. Thus, the data for permeate flux, concentration polarisation, maximum wall shear stress and Power number data presented in this paper is representative for the whole unit cell, and thus for the whole membrane module due to the periodic nature of the SWM channel.

It is worth noting that the peak frequency is associated with the shed vortices. This is because as the vortices flow downstream, the frequency of the oscillations in the *y*-direction should be the same regardless of the location of the point. As a vortex goes past a monitoring

point, first the *y*-velocity is in one direction due to the leading edge of the vortex, and then in the opposite due to the trailing edge of the vortex.

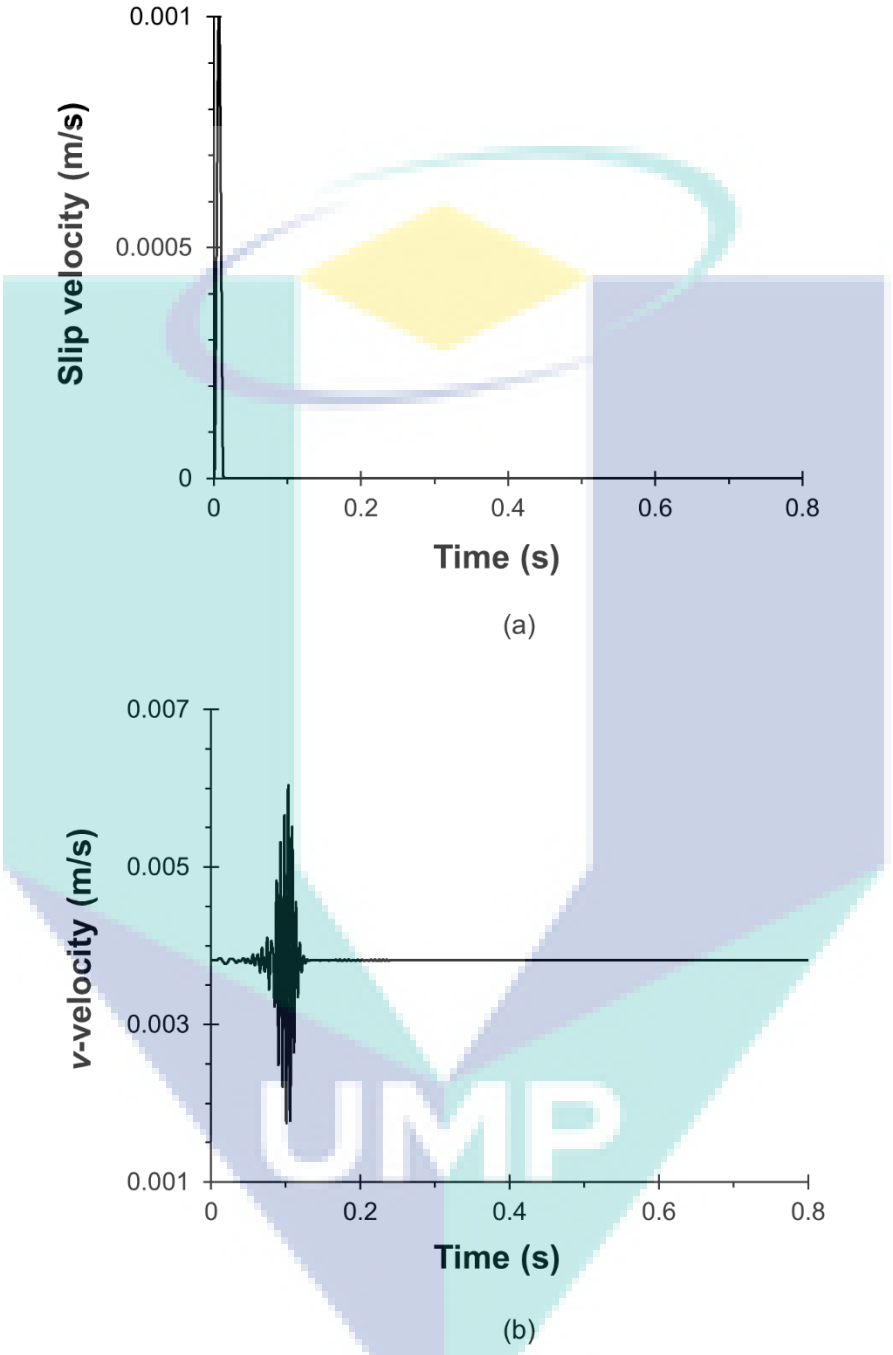

Figure 4.4: Frequency response time series for the positive pulse slip velocity stimulus and the corresponding v-velocity response at monitoring point P2, for df/hch = 0.6 and lm/hch = 4 at Re 425.

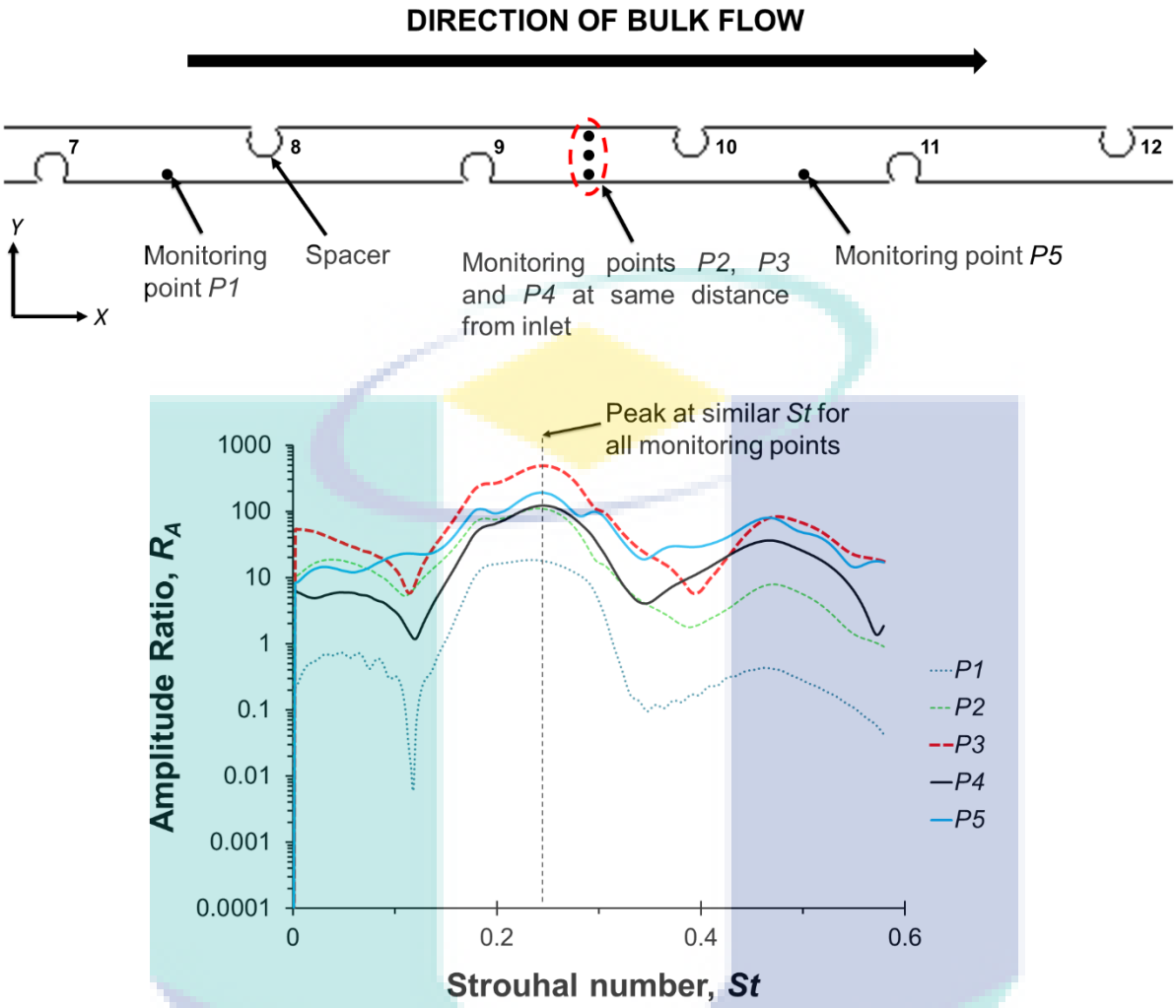

Figure 4.5: Frequency response of the pulse slip velocity at different monitoring points '•' for df/hch = 0.6 and lm/hch = 4 at Re 425.

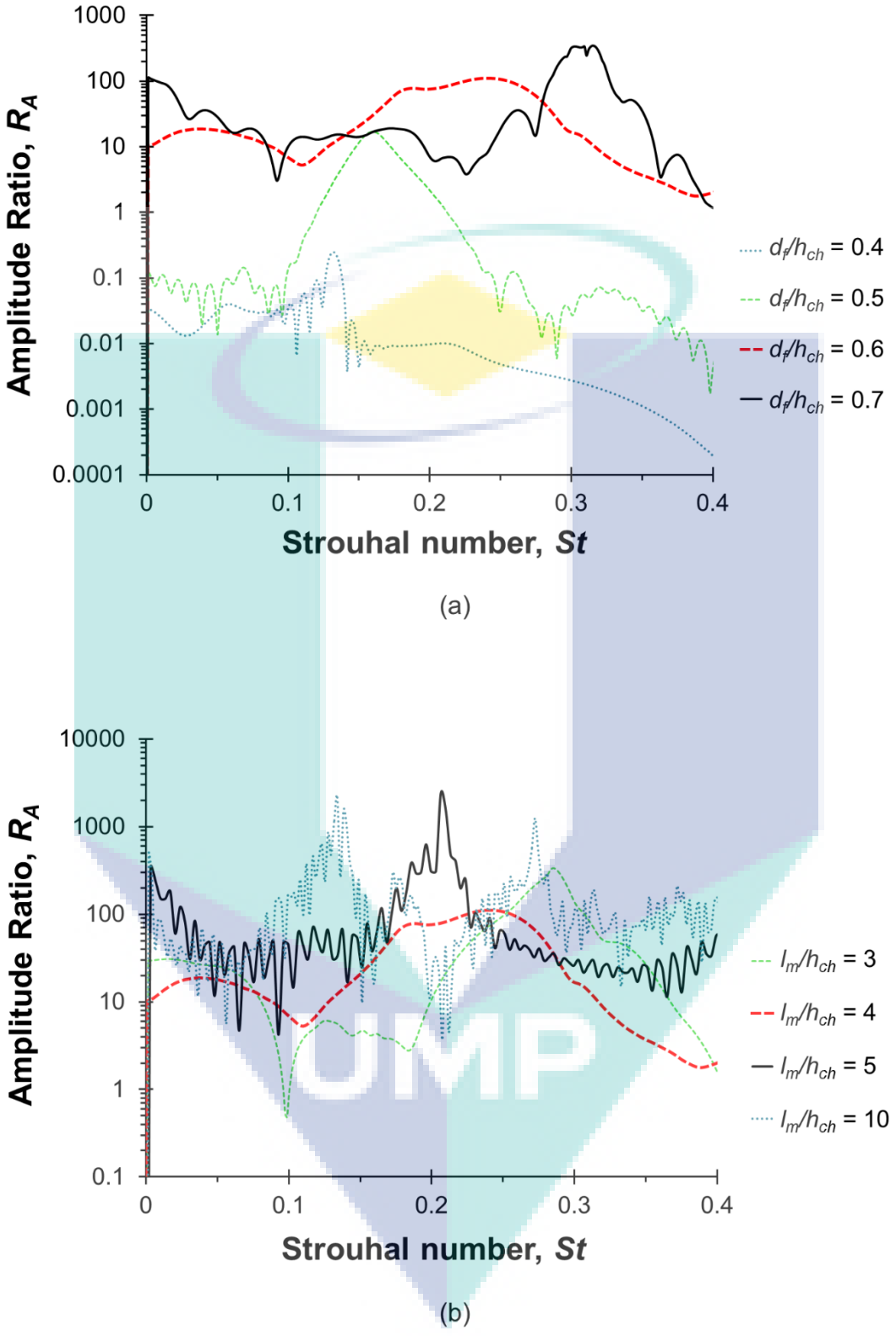

Figure 4.6: Frequency response of the pulse slip velocity at monitoring point P2 for varying (a) dimensionless spacer diameter (df/hch) at constant lm/hch = 4 and (b) dimensionless mesh length (lm/hch) at constant df/hch = 0.6 at Re 425.

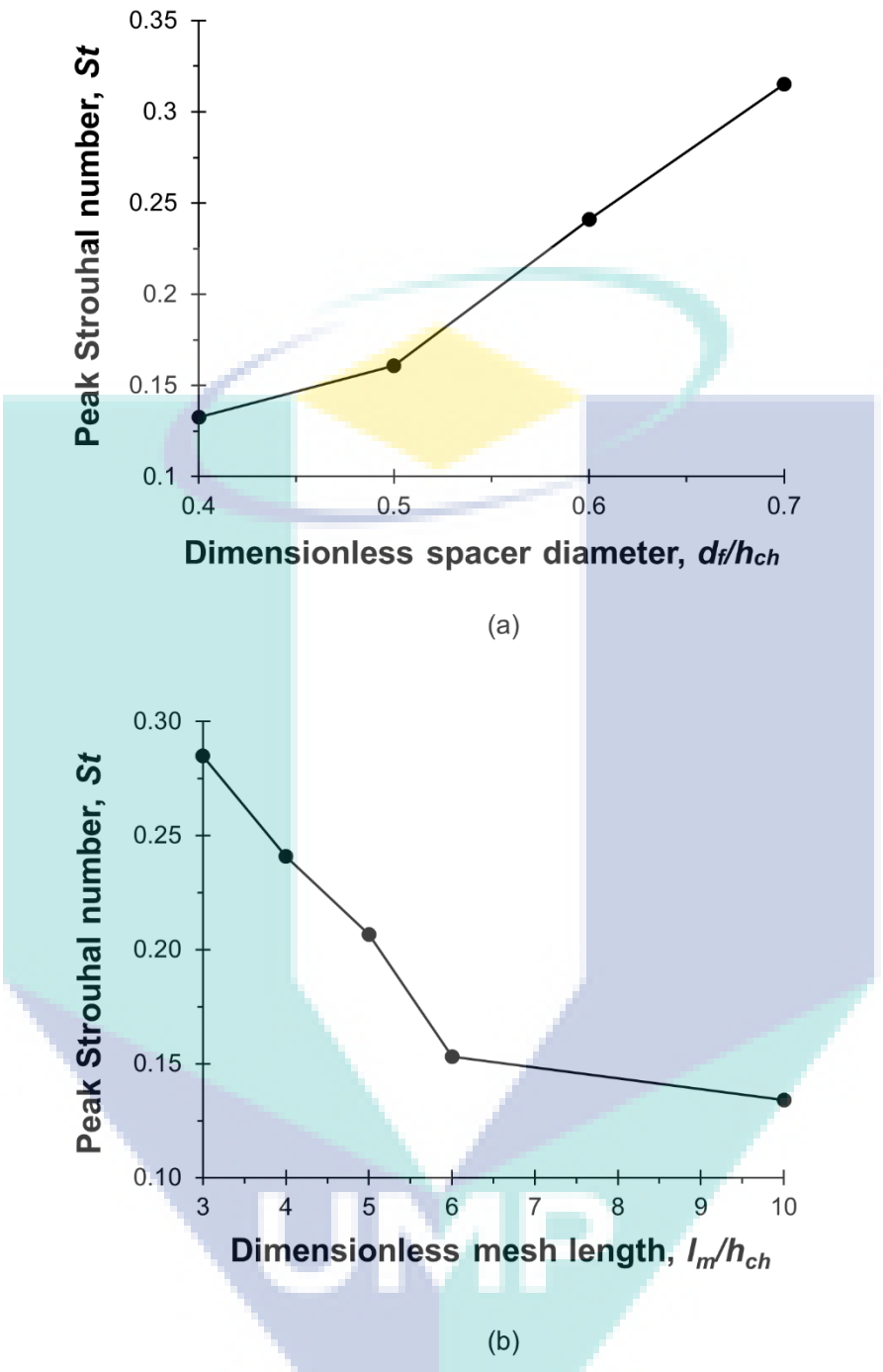

Figure 4.7: Effect of (a) dimensionless spacer diameter (df/hch) at constant lm/hch = 4 and (b) mesh length (lm/hch) at constant df/hch = 0.6 on peak Strouhal number (St) at Re 425.

Figure 4. shows that f_{pl} is significantly affected by the mesh length and filament diameter. The peak dimensionless frequency (i.e. Strouhal number) from our simulation data is about 36% higher than that reported by Fimbres Weihs and Álvarez Sánchez [58] under the same dimensionless spacer geometry ($d_f/h_{ch} = 0.6$ and $l_m/h_{ch} = 4$). The difference can be attributed to the lower Reynolds numbers ($Re_h = 350$ and 400) employed by that study, compared with Re_h = 425 used in this paper, because a larger Reynolds number typically

increases the dimensionless vortex shedding frequency [19, 58] which, for the same geometry, is proportional to the Strouhal number [71]. Thus, this provides confidence in our model prediction despite the different geometries and Reynolds number under consideration. It is worth noting that the amplitude ratio (R_A) is only a measure of how sensitive the system reacts in response to the pulse-slip input applied, which does not reflect how much flux enhancement can be achieved at this *St*.

The increasing trend in peak Strouhal number seen in Figure 4. as spacer size increases or mesh length decreases is confirmed in Figure 4.. The behaviour of the peak Strouhal number can be explained by the interaction of shear strain layers downstream the spacer. This is because the vortex shedding frequency is influenced by the roll up of the shear strain layers caused from the upstream spacer [71]. The shear strain rate is defined as:

$$\dot{\epsilon} = \frac{\partial V}{\partial n} \tag{24}$$

where V is the current linear speed of the flow at distance n from the wall.

An increase in dimensionless spacer diameter causes a reduction in the gap between spacer filament and the membrane wall, leading to a larger value of $\bar{u}_{gap}$ and an amplification of velocity oscillations (Figure 4.a). These amplified oscillations lead to shorter times required for the shear layer to roll on itself and, consequently, vortices are shed faster than for cases with a smaller spacer diameter. This explains why the peak Strouhal number increases for systems with a larger spacer diameter. Likewise, when the mesh length increases ($l_m/h_{ch} = 10$), the shear layer breaks or discontinues downstream from the spacer. This reduces the interaction of shear layer between subsequent spacers, leading to weaker vortices (Figure 4.) and eventually a smaller peak Strouhal number.

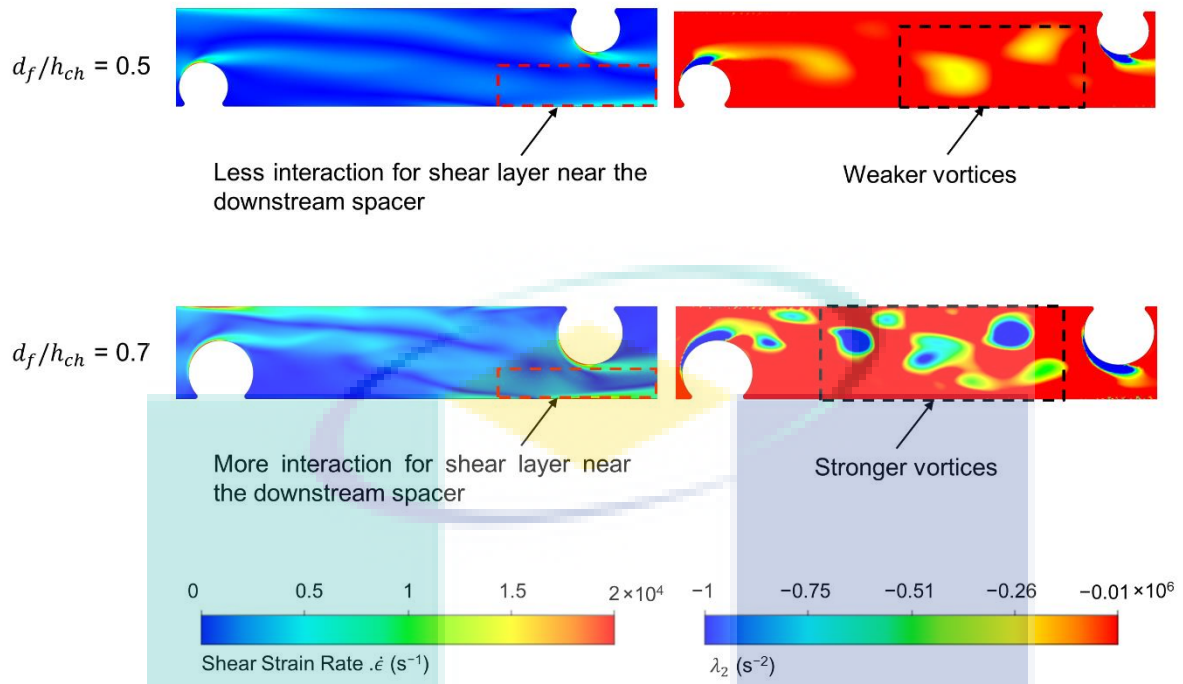

Figure 4.8: Effect of spacer diameter (df/hch) on the shear strain rate and magnitude of □2 under forced-slip at Re 425.

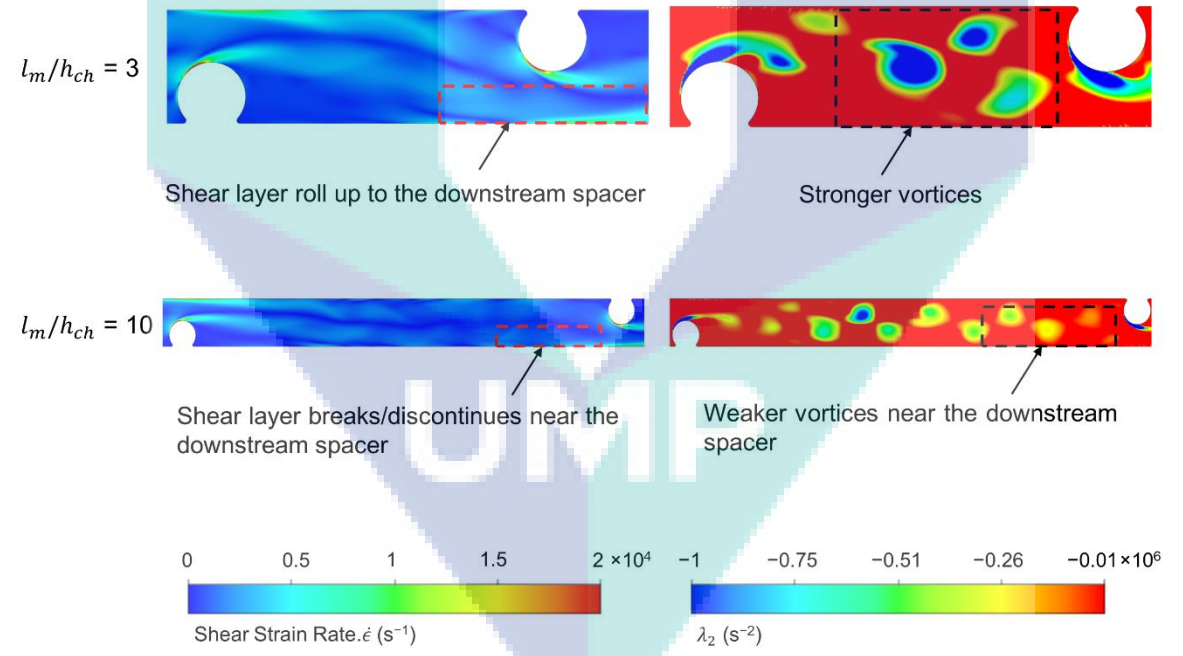

Figure 4.9: Effect of mesh length (lm/hch) on the shear strain rate and magnitude of □2 under forced-slip at Re 425.

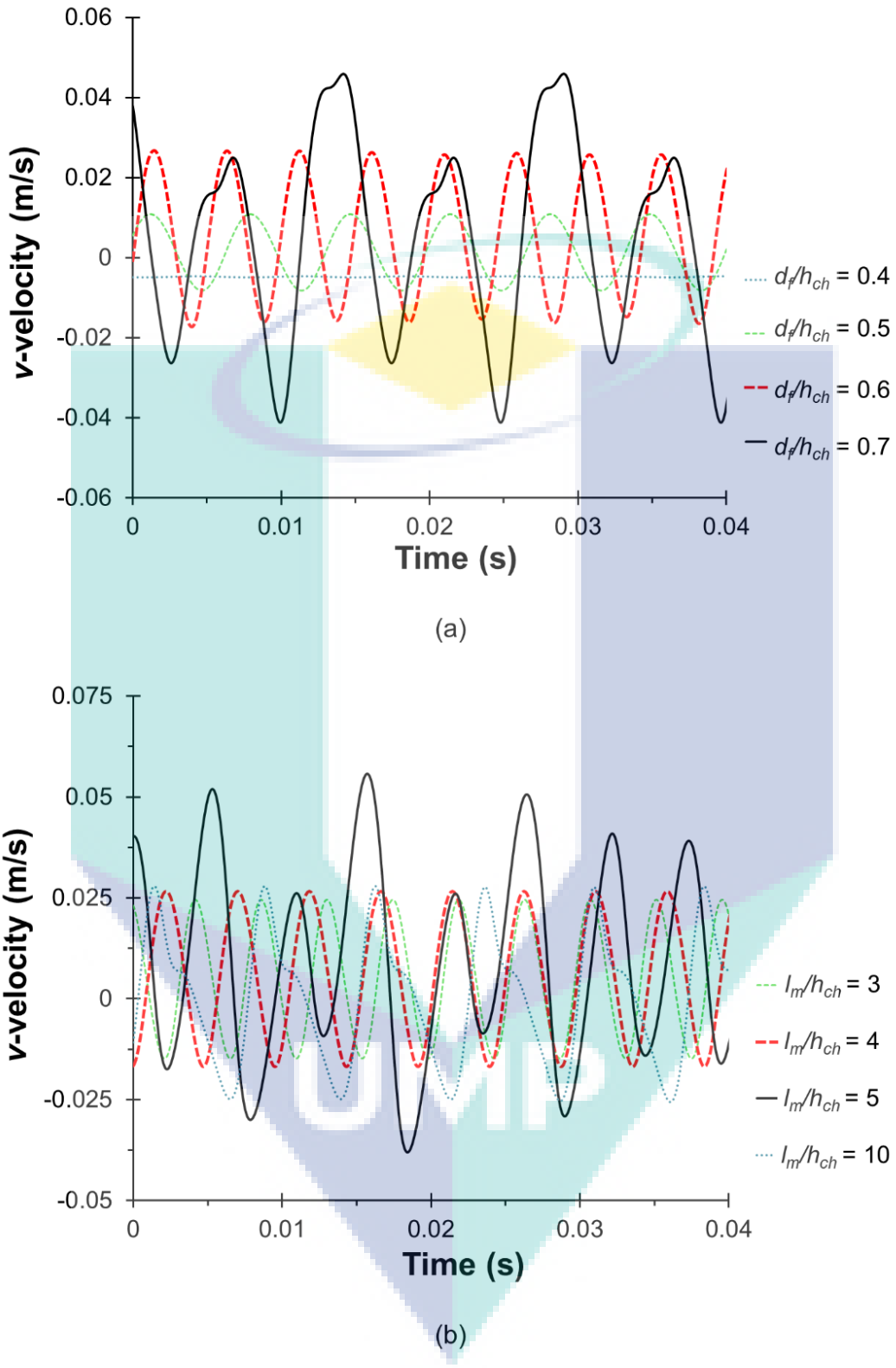

Figure 4.10: Time series v-velocity profile at monitoring point P2 for varying (a) dimensionless spacer diameter (d_f/h_{ch}) and (b) dimensionless mesh length (l_m/h_{ch}) at *Re* 425.

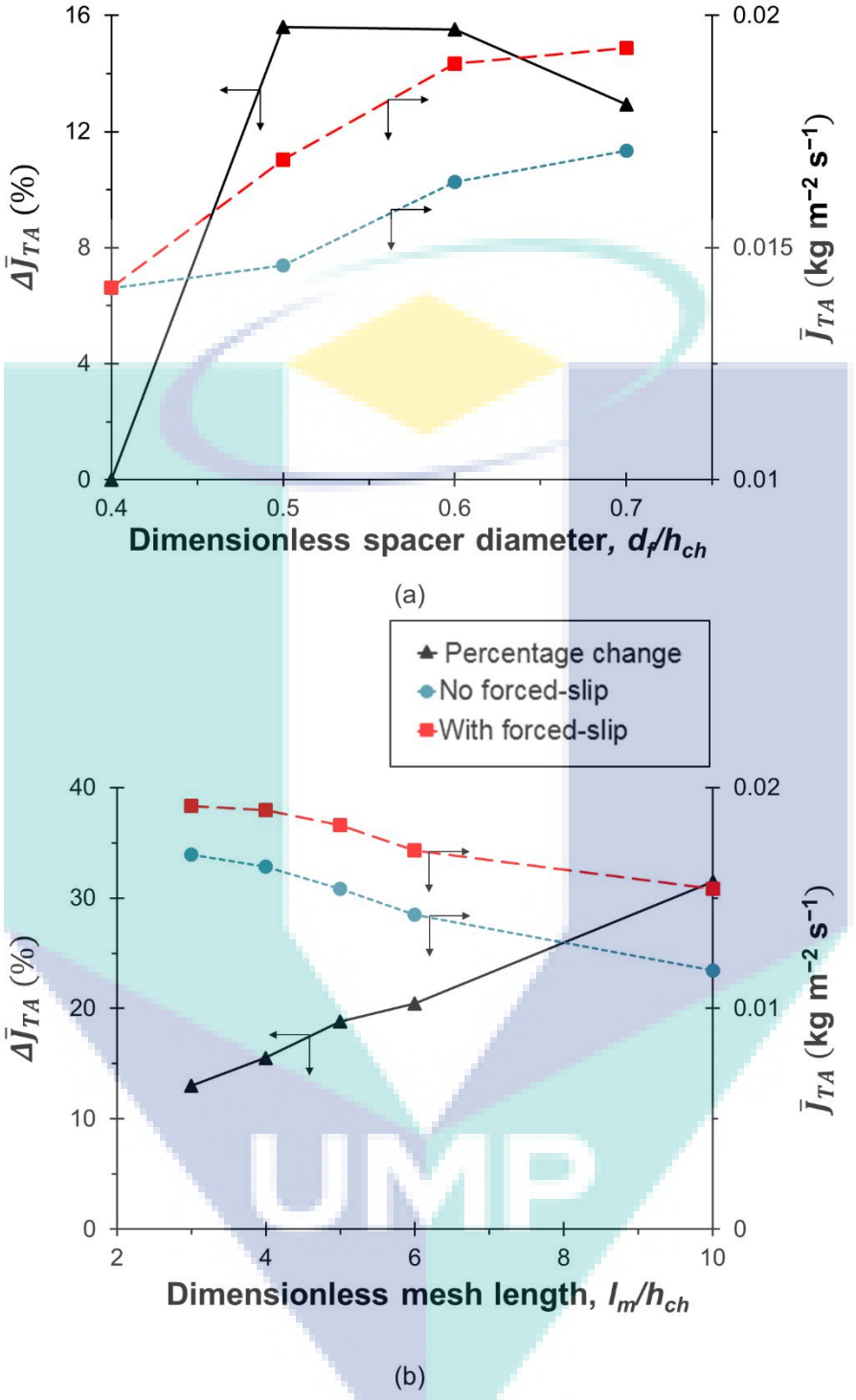

Figure 4.11: Effect of varying (a) dimensionless spacer diameter (df/hch) and (b) dimensionless mesh length (lm/hch) on the permeate flux and its percentage change due to forced-slip, for the cases without and with forced-slip at the peak frequency, at Re 425.

Figure 4.a shows that there is a peak in the relative permeate flux enhancement ($\Delta\bar{J}$) as the spacer diameter varies. The peak in $\Delta\bar{J}_{TA}$ can be explained by the relationship between vortex-shedding-induced forced-slip and the concentration polarisation (CP) modulus ($\bar{\gamma}$). At

a smaller spacer size, the system tends to dissipate energy faster to the bulk flow than for the larger spacer size. This is because the viscous force dominates over the convective force for a smaller spacer diameter (d_f/h_{ch} = 0.4), due to a smaller filament Reynolds number (i.e. $Re_f = \rho u_{avg} d_f/\mu$), which in turn dampens the flow oscillations [19] and results in a steady value for *v*-velocity (Figure 4.a). For a larger spacer, on the other hand, the system is already well-mixed as indicated by a lower CP modulus in Figure 4.a and Figure 4.0.4. Thus, the effectiveness of forced-slip in enhancing permeate flux is reduced even though the frequency of boundary layer renewal is higher (as indicated by a larger peak *St* in Figure 4.a) and the vortices are stronger (Figure 4.). In fact, it depends on the concentration polarisation of the system. This explains why forced-slip is more effective at increasing flux relative to the case without slip, for spacer diameters in the range of $0.5 < d_f/h_{ch} < 0.6$. Nevertheless, the highest flux is achieved at the largest spacer diameter considered ($d_f/h_{ch} = 0.7$), and forced-slip increases flux by just over 12% at those conditions.

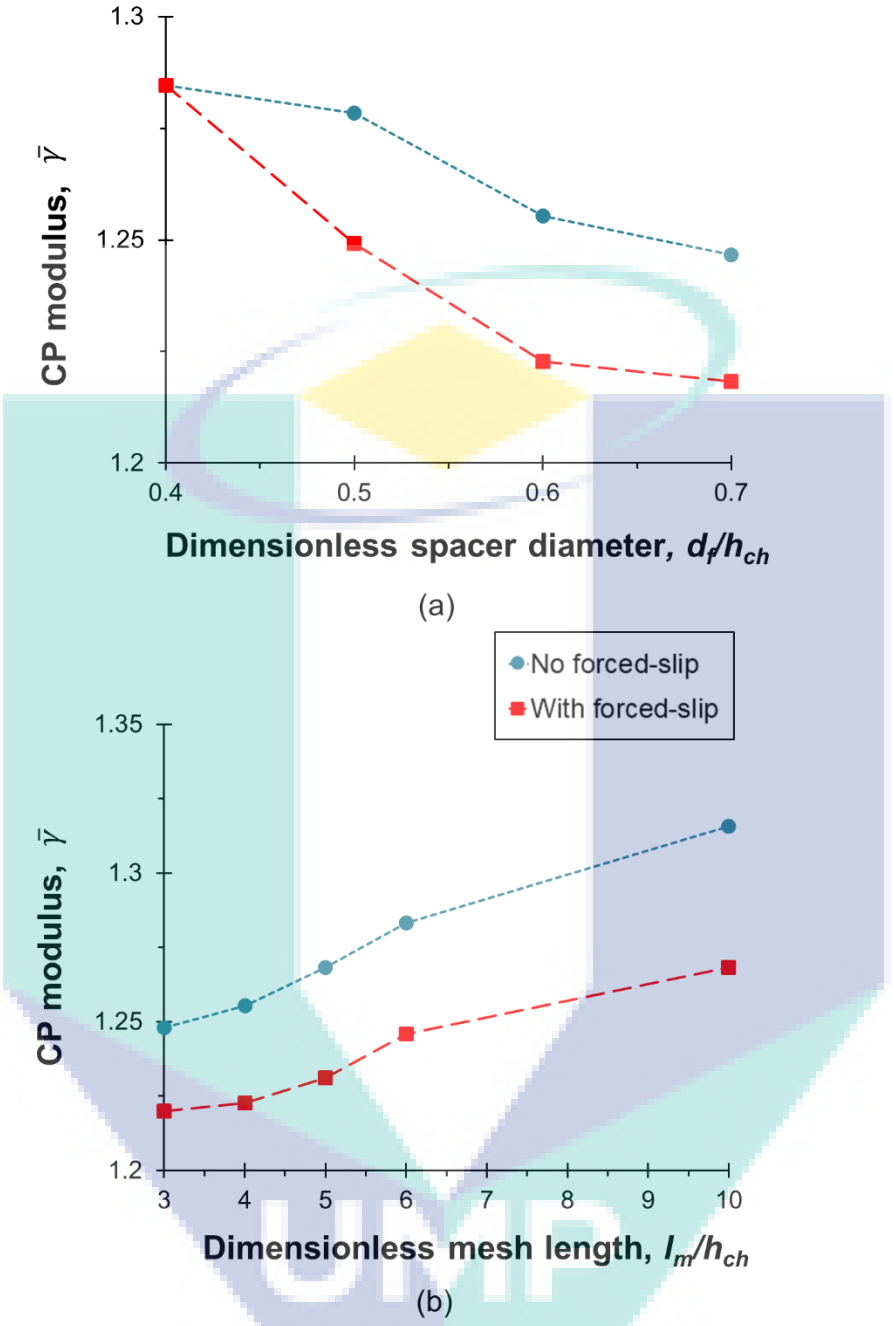

Figure 4.12: Effect of (a) dimensionless spacer diameter (df/hch) and (b) dimensionless mesh length (lm/hch) on concentration polarisation modulus ($\bar{\gamma}$), for the cases without and with forced-slip at the peak frequency, at Re 425.

In terms of the effect of mesh length, it can be seen from Figure 4.b that relative permeate flux enhancement due to forced-slip increases as mesh length increases. This is because for a larger mesh length, the CP modulus is larger (Figure 4.b and Figure 4.0.5) which in turn increases the effectiveness of forced-slip in enhancing mass transfer. Figure 4.b also shows that, as mesh length increases, flux enhancement due to forced-slip also increases albeit the actual flux decreases. This is because the boundary layer is more developed for a longer

distance between spacers, leading to lower flux without forced-slip, so the perturbations cause a significant reduction in CP due to increased boundary layer renewal. The figure also confirms that a similar permeate flux can be achieved using a larger mesh lengh (i.e. l_m/h_{ch} = 10) when forced-slip is applied, when compared to case without forced-slip at a smaller mesh length (i.e. l_m/h_{ch} = 5).

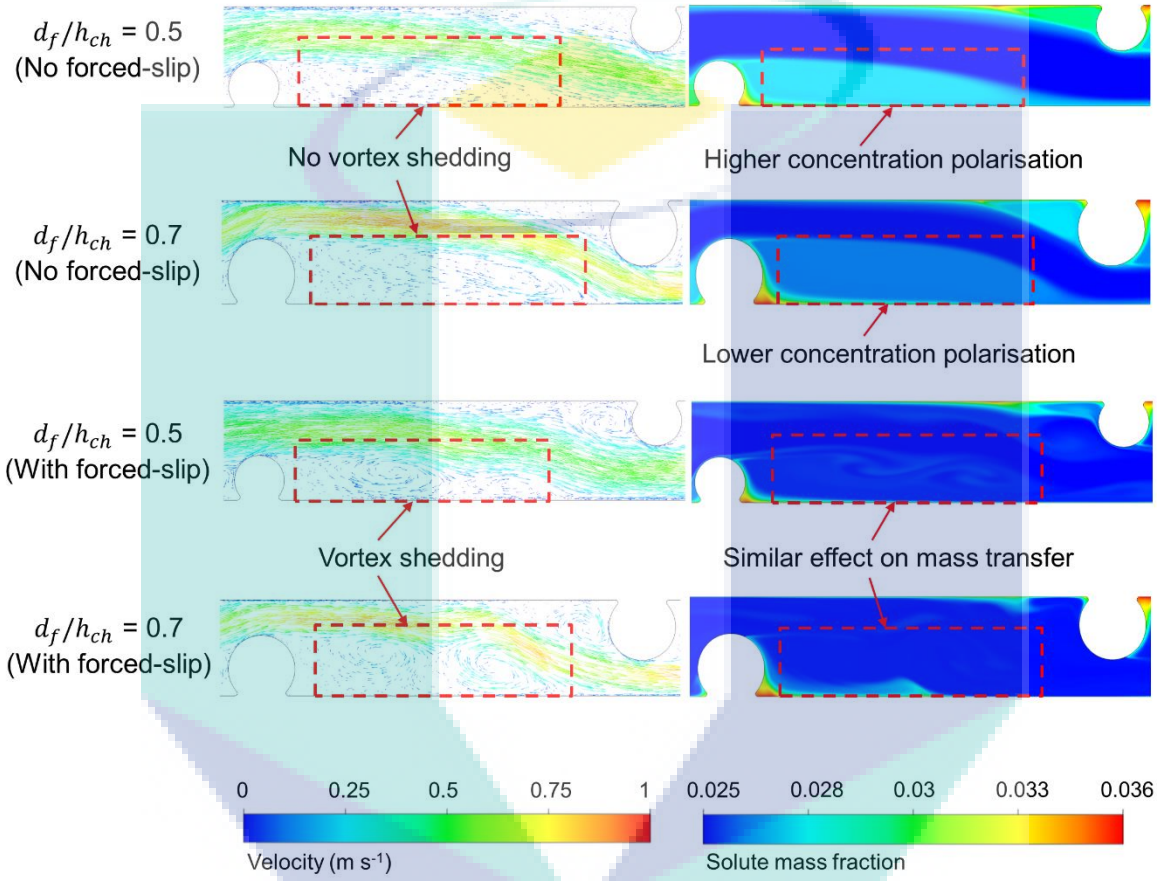

Figure 4.0.4: Effect of dimensionless spacer diameter (df/hch) on the velocity and solute concentration profiles without and with forced-slip at the peak frequency, at Re 425.

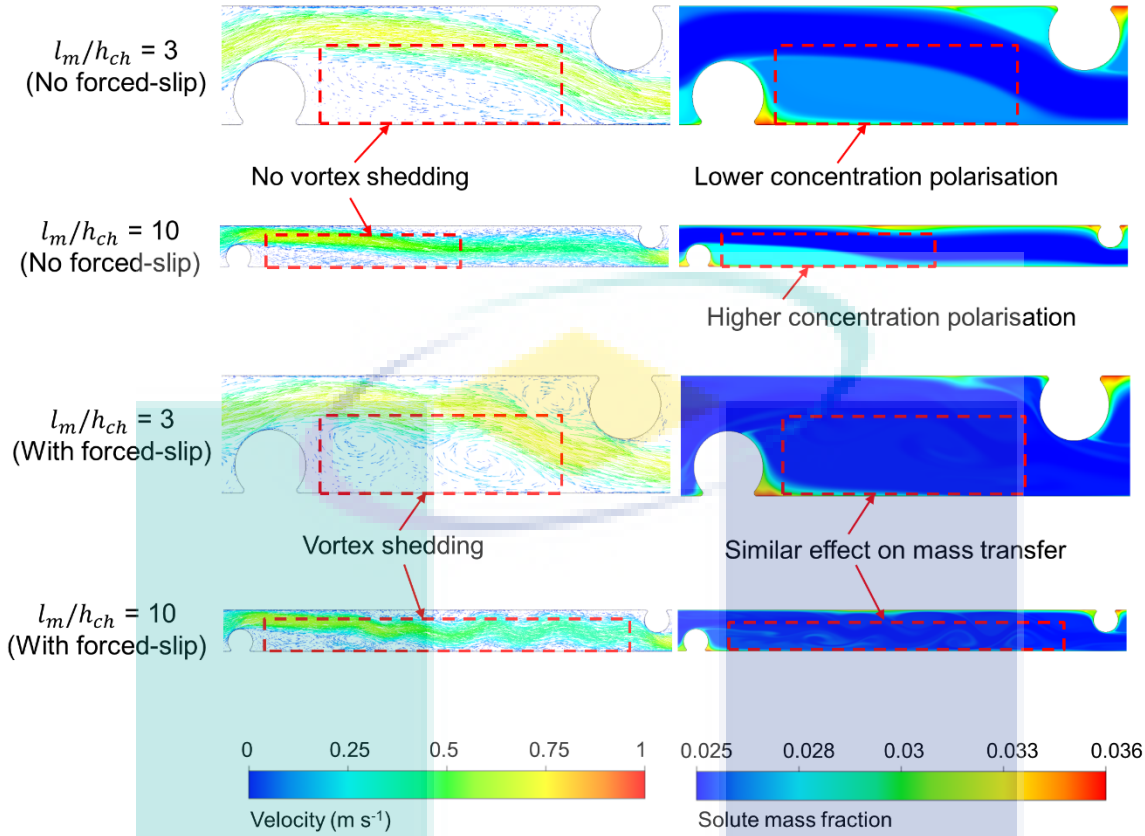

Figure 4.0.5: Effect of mesh length (lm/hch) on the velocity and solute concentration profiles without and with forced-slip at the peak frequency, at Re 425.

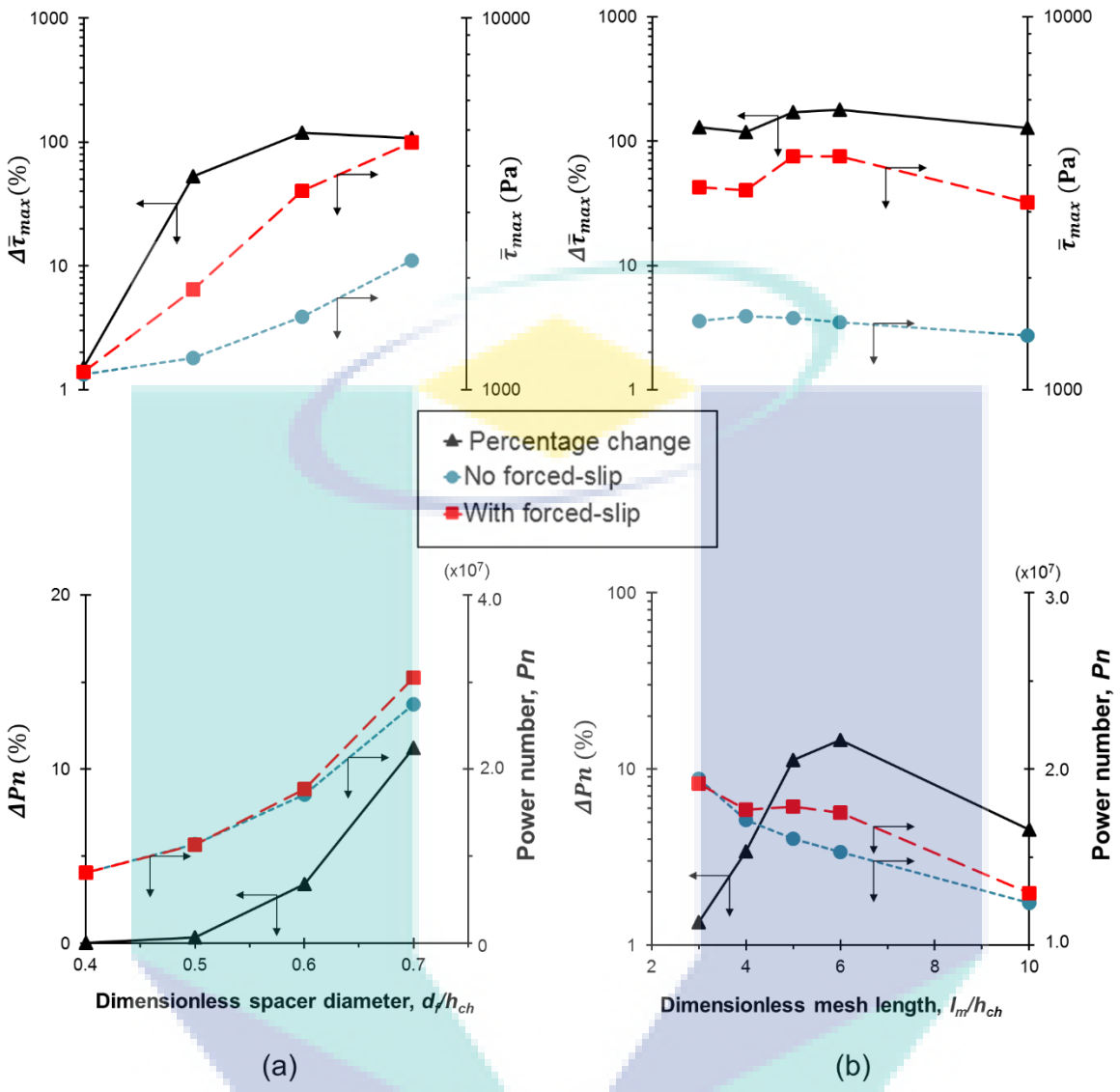

Figure 4.0.6: Effect of (a) dimensionless spacer diameter (df/hch) and (b) dimensionless mesh length (lm/hch) on the percentage change in maximum shear stress and Power number, without and with forced slip at the peak frequency, at Re 425.

Results from Figure 4.0.6a show that in the presence of forced-slip, a larger spacer diameter results in a larger increase in wall shear stress $\left(\Delta\overline{\tau}_{max}\right)$, but the increasing tendency stalls at the largest spacer diameter simulated. A higher $\overline{\tau}_{max}$ for a larger spacer is also corroborated by the larger pumping energy requirement shown in Figure 4.0.6a. On the other hand, Figure 4.0.6b shows that mesh length only has a small effect on the increase in $\overline{\tau}_{max}$; nonetheless, forced-slip causes $\overline{\tau}_{max}$ to increase over 110%, thus indicating the potential of forced-slip in reducing the tendency for fouling. It is also interesting to note that there is a maximum in ΔPn for the mesh length range under consideration. At a smaller mesh length, ΔPn increases because the form drag due to vortex-shedding-induced forced-slip dominates.

This is corroborated with the data shown in Figure 4.b, which shows the largest amplitude of *v*-velocity is observed in the middle of the mesh length range (i.e. around $l_m/h_{ch} = 5$). However, at a larger mesh length (i.e. $l_m/h_{ch} = 10$), the flow becomes less dependent on the preceding spacer and behaves closer to flow in an empty channel, which in turn reduces the intensity of form drag due to the interaction between subsequent spacers. This explains why the interaction between subsequent spacers becomes weaker for systems with larger l_m/h_{ch}, and the resulting *v*-velocity variations are smaller. This is confirmed by Figure 4., where it can be seen that the vortices lose strength as they travel downstream when the mesh length is longer. Thus, forced-slip does not substantially increase the pressure loss at a larger mesh length despite the occurrence of vortex shedding.

4.4 Conclusion

The results presented in this paper show that the resonant frequency for hydrodynamic perturbations in a spacer-filled membrane channel is significantly affected by the spacer geometric parameters, thereby affecting mixing and mass transfer enhancement. Frequency response analysis found that the resonant frequency, which is related to the vortex shedding frequency and Strouhal number, increases as the spacer diameter is increased or the mesh length is decreased, relative to the channel height. The increase in Strouhal number can be explained by the stronger shear layer interaction downstream the spacer filament, in which the vortices are being shed faster and are stronger. The opposite trend is obtained for systems with a weaker shear layer interaction downstream the spacer.

Data analysis found that an oscillating forced-slip is most effective at increasing permeate flux for spacer diameters in the middle of the range tested ($0.5 < d_f/h_{ch} < 0.6$). This is due to the trade-off between mixing-induced forced-slip and the CP modulus. Interestingly, it was observed that vortex shedding is suppressed for smaller spacer sizes ($d_f/h_{ch} \leq 0.4$), because viscous forces dominate over convective forces due to a smaller filament Reynolds number. A larger mesh length, on the other hand, the effectiveness of forced-slip in enhancing mass transfer increases because for this case vortex shedding disrupts a more developed concentration boundary layer, albeit the actual flux is smaller. Thus, the overall results reinforce the findings that hydrodynamic perturbation techniques are more effective in enhancing mass transfer for spacer designs with poor mixing (i.e. large CP).

It should be noted that all the simulations under considerations are carried out at fixed operating conditions and model parameters. Results may vary depending on parameters specified. It is also important to note that only a conventional spacer geometry (simple 2D dual-

layer) is studied in this paper. 3D effects not considered in this study (such as vortex stretching and 3D instabilities) may promote greater hydrodynamics-perturbation-induced mass transfer enhancement, especially in combination with advanced spacer designs (e.g. triple-layer or non-circular filament profiles). Future studies on this topic are therefore required.

Acknowledgements

The authors acknowledge funding support provided by Universiti Malaysia Pahang research grants (Project number RDU170324), CONACYT (PDCPN 2015-1221 and Cátedras Project 2338) and by the Instituto Tecnológico de Sonora through a PROFAPI fund (Project 2019-0054). One of us (K.F) gratefully acknowledges scholarship funding by Universiti Malaysia Pahang (UMP).

GENERAL CONCLUSION

For lower Reynolds numbers where there is no vortex shedding, non-sinusoidal waveforms with a sudden decrease in slip velocity lead to an increase in maximum wall shear. Therefore, these types of waveforms might be particularly suited for maximising wall shear for systems with low Reynolds number (e.g. high viscosity or low feed flow rate systems). It may be possible that other techniques (i.e. vibration) can also be used for generating forced velocity in the vicinity of membrane surface to improve mixing and mass transfer enhancement.

The results presented in this paper also found that if the channel peak/resonant frequency is known, applying the perturbations near the concentration boundary layer is more energy efficient than oscillating the bulk flow. This is because less energy is required to change the momentum of the smaller volume of fluid within the thin boundary layer. The data presented in this paper also confirm that white noise perturbations can be used to induce boundary layer renewal and vortex shedding without the need to identify the peak/resonant frequency *a-priori*. The occurrence of vortex shedding when applying white noise perturbations suggests that the membrane channel tends to promote the amplification of specific frequency oscillations, even though the white noise input contains many other frequencies with equal intensity. However, using white noise for perturbing the feed flow requires significantly more pumping energy than any single-sinusoidal flow perturbation approach. This implies that most of the energy in white noise perturbations is dissipated in the channel and hence wasted, because only a single frequency is important for enhancing mass transfer.

In addition, frequency response analysis found that the resonant frequency, which is related to the vortex shedding frequency and Strouhal number, increases as the spacer diameter is increased or the mesh length is decreased, relative to the channel height. The increase in Strouhal number can be explained by the stronger shear layer interaction downstream the spacer filament, in which the vortices are being shed faster and are stronger. The opposite trend is obtained for systems with a weaker shear layer interaction downstream the spacer.

Recommendations

The following recommendations are recommended for future works:

- 3D studies (such as vortex stretching and 3D instabilities) especially in combination with advanced spacer designs involving forced-slip

- Study into non-circular spacer for optimising potential of mass transfer enhancement

References

[1] TWTP, Water treatment market overview, Europe, in, The Water Treatment Plant, 2011.
[2] P.R. Neal, H. Li, A.G. Fane, D.E. Wiley, The effect of filament orientation on critical flux and particle deposition in spacer-filled channels, J. Membr. Sci., 214 (2003) 165-178.
[3] S.N. Jagannadh, H.S. Muralidhara, Electrokinetics methods to control membrane fouling, Industrial & Engineering Chemistry Research, 35 (1996) 1133-1140.
[4] F. Zamani, J.W. Chew, E. Akhondi, W.B. Krantz, A.G. Fane, Unsteady-state shear strategies to enhance mass-transfer for the implementation of ultrapermeable membranes in reverse osmosis: A review, Desalination, 356 (2015) 328-348.
[5] G.A. Fimbres-Weihs, D.E. Wiley, Numerical study of mass transfer in three-dimensional spacer-filled narrow channels with steady flow, Journal of Membrane Science, 306 (2007) 228-243.
[6] H.-y. Li, C.D. Bertram, D.E. Wiley, Mechanisms by which pulsatile flow affects cross-flow microfiltration, AIChE Journal, 44 (1998) 1950-1961.
[7] S.J. Khan, C. Visvanathan, Influence of mechanical mixing intensity on a biofilm structure and permeability in a membrane bioreactor, Desalination, 231 (2008) 253-267.
[8] P. Sui, X. Wen, X. Huang, Feasibility of employing ultrasound for on-line membrane fouling control in an anaerobic membrane bioreactor, Desalination, 219 (2008) 203-213.
[9] M.Y. Jaffrin, Dynamic shear-enhanced membrane filtration: A review of rotating disks, rotating membranes and vibrating systems, Journal of Membrane Science, 324 (2008) 7-25.
[10] R. Bian, K. Yamamoto, Y. Watanabe, The effect of shear rate on controlling the concentration polarization and membrane fouling, Desalination, 131 (2000) 225-236.
[11] M. Al-haj Ali, A. Ajbar, E. Ali, K. Alhumaizi, Optimization-based periodic forcing of RO desalination process for improved performance, Desalination and Water Treatment, 51 (2013) 6961-6969.
[12] X. Du, Y. Wang, G. Leslie, G. Li, H. Liang, Shear stress in a pressure-driven membrane system and its impact on membrane fouling from a hydrodynamic condition perspective: a review, Journal of Chemical Technology & Biotechnology, 92 (2016) 463-478.
[13] V.G.J. Rodgers, R.E. Sparks, Effect of transmembrane pressure pulsing on concentration polarization, J. Membr. Sci., 68 (1992) 149-168.
[14] A. Alexiadis, J. Bao, D.F. Fletcher, D.E. Wiley, D.J. Clements, Analysis of the dynamic response of a reverse osmosis membrane to time-dependent transmembrane pressure variation, Industrial & Engineering Chemistry Research, 44 (2005) 7823-7834.
[15] Y.Y. Liang, G. Fimbres Weihs, R. Setiawan, D. Wiley, CFD modelling of unsteady electro-osmotic permeate flux enhancement in membrane systems, Chemical Engineering Science, 146 (2016) 189-198.
[16] G.A. Fimbres-Weihs, D.E. Wiley, Review of 3D CFD modeling of flow and mass transfer in narrow spacer-filled channels in membrane modules, Chemical Engineering and Processing: Process Intensification, 49 (2010) 759-781.
[17] Y.Y. Liang, G.A. Fimbres Weihs, D.E. Wiley, Approximation for modelling electro-osmotic mixing in the boundary layer of membrane systems, J. Membr. Sci., 450 (2014) 18-27.
[18] Y.Y. Liang, M.B. Chapman, G.A. Fimbres Weihs, D.E. Wiley, CFD modelling of electro-osmotic permeate flux enhancement on the feed side of a membrane module, J. Membr. Sci., 470 (2014) 378-388.
[19] Y.Y. Liang, G.A. Fimbres Weihs, D.E. Wiley, CFD modelling of electro-osmotic permeate flux enhancement in spacer-filled membrane channels, Journal of Membrane Science, 507 (2016) 107-118.

[20] W. Li, X. Su, A. Palazzolo, S. Ahmed, E. Thomas, Reverse osmosis membrane, seawater desalination with vibration assisted reduced inorganic fouling, Desalination, 417 (2017) 102-114.
[21] H.B. Winzeler, G. Belfort, Enhanced performance for pressure-driven membrane processes: the argument for fluid instabilities, Journal of Membrane Science, 80 (1993) 35-47.
[22] N.M. Al-Bastak, A. Abbas, Periodic Operation of a Reverse Osmosis Water Desalination Unit, Separation Science and Technology, 33 (1998) 2531-2540.
[23] O. Kedem, A. Katchalsky, Thermodynamic analysis of the permeability of biological membranes to non-electrolytes, Biochimica et Biophysica Acta, 27 (1958) 229-246.
[24] D.E. Wiley, D.F. Fletcher, Techniques for computational fluid dynamics modelling of flow in membrane channels, Journal of Membrane Science, 211 (2003) 127-137.
[25] D.F. Fletcher, D.E. Wiley, A computational fluids dynamics study of buoyancy effects in reverse osmosis, Journal of Membrane Science, 245 (2004) 175-181.
[26] Y.Y. Liang, M.B. Chapman, G.A. Fimbres Weihs, D.E. Wiley, CFD modelling of electro-osmotic permeate flux enhancement on the feed side of a membrane module, Journal of Membrane Science, 470 (2014) 378-388.
[27] H.-C. Flemming, Reverse osmosis membrane biofouling, Experimental Thermal and Fluid Science, 14 (1997) 382-391.
[28] G.A. Fimbres-Weihs, D.E. Wiley, D.F. Fletcher, Unsteady Flows with mass transfer in narrow zigzag spacer-filled channels: A numerical study, Industrial & Engineering Chemistry Research, 45 (2006) 6594-6603.
[29] A. Antony, J.H. Low, S. Gray, A.E. Childress, P. Le-Clech, G. Leslie, Scale formation and control in high pressure membrane water treatment systems: A review, Journal of Membrane Science, 383 (2011) 1-16.
[30] G.A. Fimbres-Weihs, J. Álvarez-Sánchez, Synergies between pulsatile flow and spacer filaments in reverse osmosis modules, in: A. Maciel-Cerda (Ed.) Membranes – Materials, Simulations and Applications, Springer, Switzerland, 2017, pp. 67-75.
[31] P. Ratnayake, R. Setiawan, J. Bao, G. Fimbres-Weihs, D.E. Wiley, Spatio-temporal frequency response analysis of forced slip velocity effect on solute concentration oscillations in a reverse osmosis membrane channel, Computers & Chemical Engineering, 84 (2016) 151-161.
[32] G.A. Fimbres-Weihs, D.E. Wiley, Numerical study of two-dimensional multi-layer spacer designs for minimum drag and maximum mass transfer, J. Membr. Sci., 325 (2008) 809-822.
[33] DOW, DOW FILMTEC™ Fiberglassed Elements for Light Industrial Systems, in: The Dow Chemical Company (Ed.) Product Data Sheet, 2017.
[34] DOW, DOW FILMTEC™ SW30-8040 Seawater Reverse Osmosis Element, in: The Dow Chemical Company (Ed.) Product Information, 2018.
[35] FILMTEC, FILMTEC 8" Brackish Water RO Element Specifications, in: FilmTec Corporation (Ed.) Product Information, Minneapolis, USA, 1988.
[36] G.A. Fimbres-Weihs, & Álvarez-Sánchez, J. , Synergies between pulsatile flow and spacer filaments in reverse osmosis modules, In A. Maciel-Cerda (Ed.), Membranes - Materials, Simulations, and Applications. Switzerland: Springer., (2016).
[37] M. Gastelum Reyes, G. Fimbres Weihs, CFD Study of optimal frequency pulsatile flow for mass transfer enhancement in spacer-filled RO membrane channels, Memorias del Congreso de la Sociedad Mexicana de Ciencia y Tecnología de Membranas, 3 (2016) 19-27.
[38] S.Y. Lim, Y.Y. Liang, G.A. Fimbres Weihs, D.E. Wiley, D.F. Fletcher, A CFD study on the effect of membrane permeance on permeate flux enhancement generated by unsteady slip velocity, Journal of Membrane Science, 556 (2018) 138-145.

[39] Y.Y. Liang, G.A. Fimbres Weihs, D.F. Fletcher, CFD study of the effect of unsteady slip velocity waveform on shear stress in membrane systems, Chemical Engineering Science, 192 (2018) 16-24.
[40] W. Shi, M.M. Benjamin, Effect of shear rate on fouling in a Vibratory Shear Enhanced Processing (VSEP) RO system, Journal of Membrane Science, 366 (2011) 148-157.
[41] F. Li, W. Meindersma, A.B. De Haan, T. Reith, Novel spacers for mass transfer enhancement in membrane separations, J. Membr. Sci., 253 (2005) 1-12.
[42] P. Chakraborty, S. Balachandar, R.J. Adrian, On the relationships between local vortex identification schemes, Journal of Fluid Mechanics, 535 (2005) 189-214.
[43] K. Foo, Y.Y.Liang, G.A Fimbres Weihs, CFD study of the effect of SWM feed spacer geometry on mass transfer enhancement driven by forced transient slip velocity, Journal Membrane Science, (2018) (under review).
[44] A.H. Haidaria, S.G.J. Heijmana, W.G.J. van der Meera, Optimal design of spacers in reverse osmosis, Separation and Purification Technology, 192 (2018) 441-456.
[45] J. Schwinge, P.R. Neal, D.E. Wiley, D.F. Fletcher, A.G. Fane, Spiral wound modules and spacers: Review and analysis, Journal of Membrane Science, 242 (2004) 129-153.
[46] E. Matthiasson, B. Sivik, Concentration polarization and fouling, Desalination, 35 (1980) 59-103.
[47] R.A. Shaw, R. Deluca, W.N. Gill, Reverse osmosis: increased productivity by reduction of concentration polarization in laminar flow reverse osmosis using intermediate non-rejecting membrane sections, Desalination, 11 (1972) 189-205.
[48] J. Schwinge, D.E. Wiley, D.F. Fletcher, Simulation of Unsteady Flow and Vortex Shedding for Narrow Spacer-Filled Channels, Ind. Eng. Chem. Res., 42 (2003) 4962-4977.
[49] G. Guillen, E.M.V. Hoek, Modeling the impacts of feed spacer geometry on reverse osmosis and nanofiltration processes, Chemical Engineering Journal, 149 (2009) 221–231.
[50] J. Schwinge, D.E. Wiley, D.F. Fletcher, Simulation of the flow around spacer filaments between channel walls. 2. Mass-transfer enhancement, Ind. Eng. Chem. Res., 41 (2002) 4879-4888.
[51] H.-G. Park, S.-G. Cho, K.-J. Kim, Y.-N. Kwon, Effect of feed spacer thickness on the fouling behavior in reverse osmosis process - A pilot scale study, Desalination, 379 (2016) 155-163.
[52] A. Alexiadis, D. E. Wiley, D. F. Fletcher, J. Bao, Laminar Flow Transitions in a 2D Channel with Circular Spacers, Ind. Eng. Chem. Res., 46 (2007) 5387-5396.
[53] J. Schwinge, D.E. Wiley, D.F. Fletcher, Simulation of the Flow around Spacer Filaments between Narrow Channel Walls. 1. Hydrodynamics, Ind. Eng. Chem. Res., 41 (2002) 2977-2987.
[54] S. Kerdi, A. Qamar, J.S. Vrouwenvelder, N. Ghaffour, Fouling resilient perforated feed spacers for membrane filtration, Water Research, 140 (2018) 211-219.
[55] N. Sreedhar, N. Thomas, O. Al-Ketan, R. Rowshan, H. Hernandez, R.K. Abu Al-Rub, H.A. Arafat, 3D printed feed spacers based on triply periodic minimal surfaces for flux enhancement and biofouling mitigation in RO and UF, Desalination, 425 (2018) 12-21.
[56] Y.Y. Liang, G.A. Fimbres Weihs, D.E. Wiley, Comparison of oscillating flow and slip velocity mass transfer enhancement in spacer filled membrane channels: CFD analysis and validation, Journal of Membrane Science, (2019).
[57] X. Su, W. Li, A. Palazzolo, S. Ahmed, Concentration polarization and permeate flux variation in a vibration enhanced reverse osmosis membrane module, Desalination, 433 (2018) 75-88.
[58] G.A. Fimbres-Weihs, J. Álvarez-Sánchez, Synergies between pulsatile flow and spacer filaments in reverse osmosis modules, in: A. Maciel-Cerda (Ed.) Membranes - Materials, Simulations, and Applications, Springer, Switzerland, 2016.

[59] Y.Y. Liang, G.A. Fimbres Weihs, R. Setiawan, D.E. Wiley, CFD modelling of unsteady electro-osmotic permeate flux enhancement in membrane systems, Chemical Engineering Science, 146 (2016) 189-198.
[60] Y.Y. Liang, K.Y. Toh, G.A. Fimbres Weihs, 3D CFD study of the effect of multi-layer spacers on membrane performance under steady flow, Journal of Membrane Science, 580 (2019) 256-267.
[61] R. Iwatsu, J.M. Hyun, K. Kuwahara, Analyses of three-dimensional flow calculations in a driven cavity, Fluid Dynamics Research, 6 (1990) 91-102.
[62] G.A. Fimbres-Weihs, D.E. Wiley, Review of 3D CFD modeling of flow and mass transfer in narrow spacer-filled channels in membrane modules, Chemical Engineering and Processing: Process Intensification, 49 (2010) 759-781.
[63] G.A. Fimbres-Weihs, D.E. Wiley, D.F. Fletcher, Unsteady Flows with Mass Transfer in Narrow Zigzag Spacer-Filled Channels: A Numerical Study, Industrial & Engineering Chemistry Research, 45 (2006) 6594-6603.
[64] G.A. Fimbres-Weihs, D.E. Wiley, Numerical study of two-dimensional multi-layer spacer designs for minimum drag and maximum mass transfer, Journal of Membrane Science, 325 (2008) 809-822.
[65] O. Kedem, A. Katchalsky, Thermodynamic analysis of the permeability of biological membranes to non-electrolytes, Biochimica et Biophysica Acta, 27 (1958) 229-246.
[66] S.A. Billings, Nonlinear System Identification: NARMAX Methods in the Time, Frequency, and Spatio-Temporal Domains, Wiley, UK, 2013.
[67] Pesila Ratnayake, Ridwan Setiawan, Jie Bao, Gustavo Fimbres-Weihs, Dianne E. Wiley, Spatio-temporal frequency response analysis of forced slip velocity effect on solute concentration oscillations in a reverse osmosis membrane channel, Computers and Chemical Engineering, 84 (2016) 151-161.
[68] L.M. Surhone, M.T. Timpledon, S.F. Marseken, Strouhal Number, Betascript Publishing, Latvia, 2010.
[69] J. Jeong, F. Hussain, On the identification of a vortex, Journal of Fluid Mechanics, 285 (1995) 69-94.
[70] S. Dupont, Y. Brunet, Coherent structures in canopy edge flow: a large-eddy simulation study, Journal of Fluid Mechanics, 630 (2009) 93-128.
[71] G. Xu, Y. Zhou, Strouhal numbers in the wake of two inline cylinders, Experiments in Fluids, 37 (2004) 248-256.